



Emerging applications of MXenes for photodetection: Recent advances and future challenges

Lingfeng Gao^{1,*,#}, Yiming Zhao^{2,#}, Xiaohua Chang¹, Jian Zhang³, Ying Li², Swelm Wageh⁴, Omar A. Al-Hartomy⁴, Abdullah G. Al-Sehemi⁵, Han Zhang^{3,*}, Hans Ågren^{6,7,*}

¹ College of Material Chemistry and Chemical Engineering, Key Laboratory of Organosilicon Chemistry and Material Technology, Ministry of Education, Key Laboratory of Organosilicon Material Technology, Zhejiang Province, Hangzhou 311121, Zhejiang, PR China

² College of Chemical Engineering, Zhejiang University of Technology, Hangzhou 310014, PR China

³ College of Optoelectronic Engineering, Shenzhen University, Shenzhen 518060, PR China

⁴ Department of Physics, Faculty of Science, King Abdulaziz University, Jeddah 21589, Saudi Arabia

⁵ Research Center for Advanced Materials Science (RCAMS), King Khalid University, P.O. Box 9004, Abha 61413, Saudi Arabia

⁶ College of Chemistry and Chemical Engineering, Henan University, Kaifeng, Henan 475004, PR China

⁷ Department of Physics and Astronomy, Uppsala University, SE-75120 Uppsala, Sweden

The development and applications of transition metal carbides, nitrides and carbonitrides, commonly denoted as MXenes, have during the last few years rapidly expanded in various technological fields owing to their unique and controllable properties. These materials exhibit competing performance comparing with traditional materials and have created numerous opportunities for technology markets. Taking the advantage of excellent optoelectronic features, MXenes have been utilized for the construction of photodetectors with various structures and unique functionalities. While the application of MXenes in this area can be traced back to 2016, we have during the recent three years witnessed a dramatic development of MXene-based photodetectors, calling for a timely review to guideline their future direction. In this work, synthetic strategies of pristine MXenes are briefly introduced and their properties are discussed focusing on the optoelectronic aspects that are fundamental for the photoelectric conversion. Recent advances of MXene-based photodetectors are comprehensively summarized based on different types of MXenes and innovative designs of device construction. Finally, we provide perspectives for future challenges and opportunities of MXene-based photodetectors, which may enlighten their further development.

Keywords: MXenes; Photodetection; 2D material; Electrode; Composite

Introduction

Owing to the development of upcoming Fifth-Generation wireless networks and Internet of Things, photodetectors have generated intense interest and are by now widely investigated in

various fields such as imaging, detection, sensing and monitoring [1–3]. The applications in these fields put high requests with respect to light detection, device structure and active materials. Generally, low dimensional materials exhibit great potential for constructing various optoelectronic devices [4–6]. For instance, the in-plane transport of electrons is several orders of magnitude higher than that of out-plane transport in two-dimensional (2D) materials, resulting in a fast response in the corresponding photodetector [7]. In this context, the discovery of single-layer gra-

* Corresponding authors.

E-mail addresses: Gao, L. (gaolingfeng@hznu.edu.cn), Zhang, H. (hzhang@szu.edu.cn), Ågren, H. (hans.agren@physics.uu.se).

These authors contributed equally to the work.

phene has sparked a wave of research on 2D atomically thin materials. To date, more than 20 kinds of 2D materials have been reported based on not only single elements but also chemical compounds, and fresh ideas are now constantly being injected into the family of 2D materials.

By removing the Al layer from Ti_3AlC_2 , Naguib et al. developed a new branch of 2D materials giving the name “MXene” to emphasize the graphene-like structure [8]. In the past decade, more than 40 kinds of MXenes have been experimentally synthesized and MXene has since become an abbreviation for transition metal carbides, nitrides, and carbonitrides [9–11]. Generally, $n + 1$ layers of transition metals (M) are interleaved with n layers of carbon/nitrogen in MXenes and a universal formula of $\text{M}_{n+1}\text{X}_n\text{T}_x$ is applied considering the surficial terminations (T). Large numbers of compositional variables have endowed the achievement of specific properties and facilitated their potential applications in various fields. To date, MXenes with various dimensions have been achieved based on front-side design and post-modification, and have been utilized for networks, nanowires, quantum dots, *etc* [12–14]. As firmly demonstrated, MXenes exhibit many intriguing properties such as excellent transmittance, mechanical flexibility, high conductivity, tunable work functions, which can be tuned via internal composition and surficial terminations. Enlightened by these fascinating properties, photodetectors based on MXene materials have attracted tremendous attention for synthesis and use.

Generally, photodetectors are fundamental optoelectronic devices with the ability to convert the incident light radiation into electrical signals for further processing, while 2D materials are widely applied as building blocks for their construction. For instance, graphene shows high carrier mobility while also zero band gap and low absorbance that inhibit their further application in photodetection [15]. Transition metal dichalcogenides exhibit direct band gaps when the thickness is reduced to a monolayer, while their carrier mobilities are about three orders lower than that of graphene [16]. The recently investigated phosphorene exhibits anisotropic light-matter interactions and a thickness-dependent band-gap range (0.3–2.0) that is suitable for infrared photodetectors [17]. However, phosphorene suffers from irreversible oxidization under ambient conditions, leading to the inevitable issue of long-term cycling instability for the resultant photodetectors [18]. In order to meet the requirements for commercial applications, great efforts have been made for searching novel 2D materials and device configurations for achieving high-performance. Compared with the aforementioned 2D materials, MXenes with different elements can be fabricated in large-scale with low cost. Their excellent electric and optical properties also lay the foundation for high performance optoelectronic devices. The direct utilization of MXenes as active materials in constructing various photodetectors have been extensively investigated in the recent five years, serving as electrodes to mention one out of many examples [19–21]. In addition to the traditional FET-type construction, several novel structures have also been developed such as capacitive-, photothermal-, and photoelectrochemical type photodetectors, which further have extended their practical applications. Fig. 1a summarizes the publications of MXene-based photodetectors as function of years, where the primal investigation can be

traced back to 2016 [22]. The number of publications have dramatically increased in the recent three years (more than 70%), indicating that MXene-based photodetectors have undergone a rapid development since 2020. This can be ascribed to the mature fabrication strategies and increased variation of MXene materials as well as to the improvement of device design. At the early stage, MXenes were predominantly applied as electrodes, owing to their controllable optical and electric properties. Recently, pristine MXenes and their composites have more commonly been utilized as active materials taking advantage of synergistic effects of self-power, flexibility, narrowband feature, solar blinding and two-sided responses. As can be seen in the summarized pie chart, more than 80% of the applications of MXene species have been focused on the firstly discovered $\text{Ti}_3\text{C}_2\text{T}_x$ MXene while the photo-response performance by now also include a number other types of MXenes, such as Mo_2CT_x , Nb_2CT_x , $\text{Sc}_x\text{-CT}_x$, and Ti_2CT_x .

Undoubtedly, the research on MXene-based photodetectors is still at its infancy with much remaining potential applications to be further exploited. There exist two review articles summarizing MXene-based photodetectors, focusing on their photo-response performance. However, the detailed roles of MXene in these photodetectors have not been classified and the recently discovered device constructions are not included. According to the summarized publication tendency, more than half of the publications are reported in 2021–2022, indicating that the applications of MXenes in photodetectors have become a research hotspot. Therefore, we believe that the important implications of the booming MXene-based photodetection field calls for a timely review of the most advanced development to help streamline further efforts. To this end, we provide here a comprehensive summary for the burgeoning progress of MXene-based photodetectors, and offer an overview of their applications (Fig. 1b). We first discuss the synthetic strategies of pristine MXenes and their properties, mainly focusing on the optical and electric properties essential for their photoresponse performance. The constructions of MXene-based photodetectors are summarized regarding the roles of MXenes, including electrode and active materials (both pristine MXenes and their composites). Finally, a perspective outlook for future challenges of MXene-based photodetectors is provided. We envisage that this review could be a timely contribution that helps understand the position of MXenes in the field of photodetection and that also can provide guidelines for the further design of MXene-based photodetectors with high performance.

Preparation of MXenes

Generally, the preparation of MXenes can be classified by two main strategies, named as top-down and bottom-up. For the top-down approach, MXenes are obtained from their MAX precursor, which has the general formula of $\text{M}_{n+1}\text{AX}_n$ ($n = 1, 2, 3$ or 4). The synthesized MXenes have various surface terminations such as $-\text{F}$, $-\text{OH}$, $-\text{O}$ groups, which though often are difficult to chemically control. On the other hand, the bottom-up method endows MXene tunable terminations and pristine MXene without the generation of special surface groups. It also gives lateral sizes that are larger compared with those from the top-down

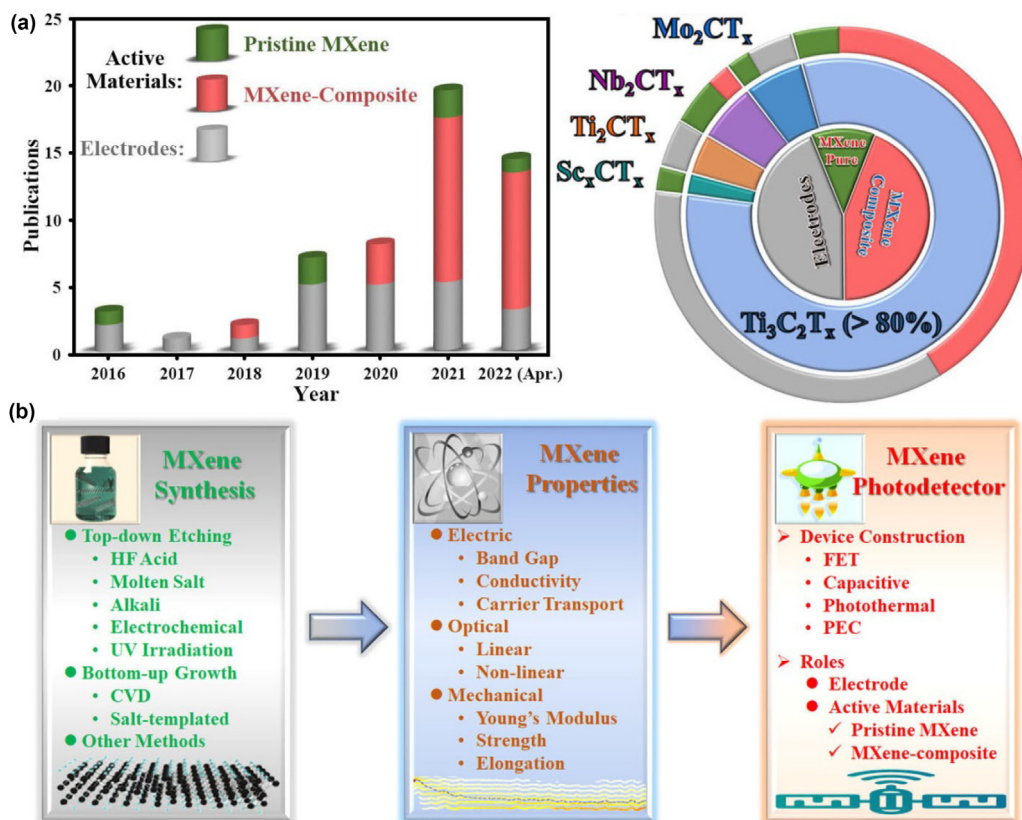


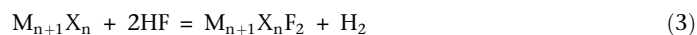
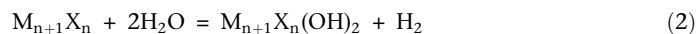
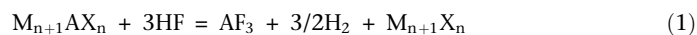
FIGURE 1

(a) Summarized publication trends for MXene-based photodetectors and a corresponding pie chart for the respective proportions based on various MXenes. (b) A brief content summary of this review article.

approach, so facilitating the investigation of their intrinsic properties. Also other approaches have been proposed for several specific MXenes, that have further extended the MXene family. To date, there are about 40 kinds of MXenes that have been experimentally synthesized while hundreds of possible MXenes have been predicted by theoretical simulations.

Top-down strategy

Hydrofluoric Acid (HF) Etching. Taking the advantage of chemical activity of the metallic M-A bonds, MXenes can be obtained by selective etching of the “A” layers from the MAX phases with strong acid. For instance, the initial Ti_3C_2 MXene was obtained from Ti_3AlC_2 by HF etching in 2011 (Fig. 2a) [8]. Generally, the reaction mechanism can be explained as follows:



The “A” element in the MAX phase can be removed by the HF acid. According to the chemical reactions, MXenes are more commonly represented as $\text{M}_{n+1}\text{X}_n\text{T}_x$, where T represents the abundant terminations. In addition to the general ternary stoichiometric MXenes, nonstoichiometric MXenes with double transition metals or carbonitrides can also be obtained from their

MAX counterparts. Fig. 2b indicates the formation of MXene alloys with varying degrees of ordering, where the $(\text{Ti}_{1/3}\text{Mo}_{2/3})_3\text{C}_2$ MXene is predicted to be the easiest to synthesize [23]. Furthermore, the HF etching method can be used to fabricate several MXenes from non-MAX phases such as $\text{Mo}_2\text{Ga}_2\text{C}$, $\text{Zr}_3\text{Al}_3\text{C}_5$, ScAl_3C_3 , and $\text{Hf}_3[\text{Al}(\text{Si})_4\text{C}_6]$ [24–27]. As shown in Fig. 2c, the first Mo-based MXene (Mo_2C) was obtained from the $\text{Mo}_2\text{Ga}_2\text{C}$ phase by etching with 50% HF acid, which further unlocked many potential applications of Mo-based MXenes [24].

Modified Acid Etching. Considering the relatively high toxicity of HF acid, bi-fluoride etchants have been demonstrated as substitutes during the etching process. For instance, Halim et al. successfully fabricated Ti_3C_2 by the use of NH_4HF_2 and the NH_4HF_2 -etched Ti_3C_2 showed excellent thermal stability compared to that of HF-etched Ti_3C_2 [28]. Moreover, etching of $\text{Ti}_3\text{C}_2\text{T}_x$ can be achieved in a polar organic solvent with the assistance of NH_4HF_2 [29]. In addition, HF acid can be produced in-situ via the combination of fluoride salts and hydrochloric acid (HCl), which also can be used to etch MAX phases. As revealed by Ghidui et al., a novel approach has been developed to synthesize high-yield MXenes by the mixture of HCl and lithium fluoride (LiF) [30]. As shown in Fig. 2d, the size of MXene flake increases with the increment of $\text{LiF}/\text{Ti}_3\text{AlC}_2$ $\text{HCl}/\text{Ti}_3\text{AlC}_2$ ratios since the superfluous HCl facilitates aluminum etching [22]. Furthermore, other fluoride salts (such as NaF, KF, Fe_3F , CsF and CaF_2) can also be used to fabricate MXenes by mixing with

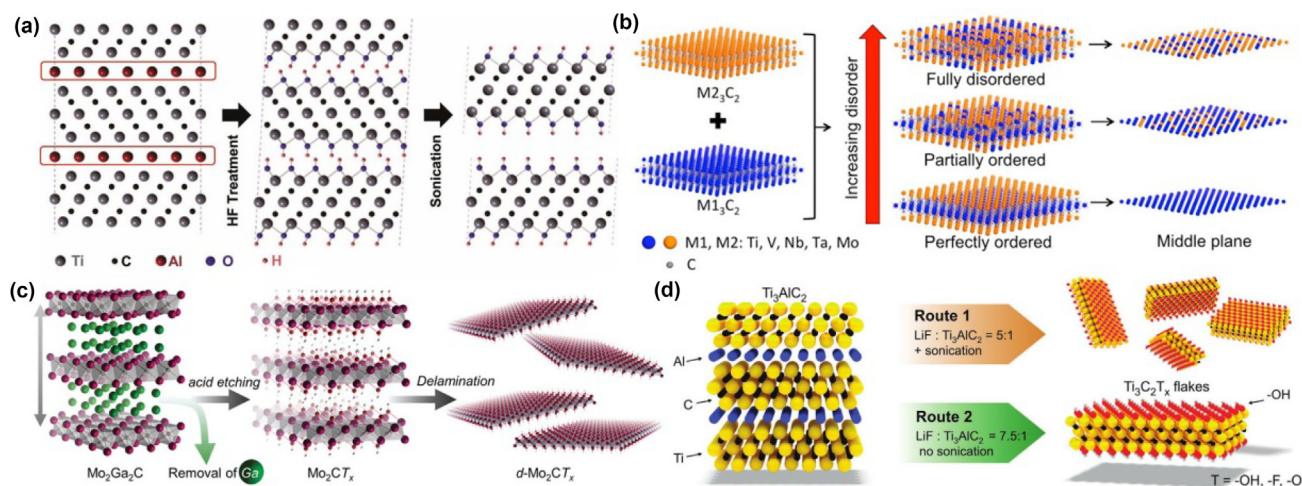


FIGURE 2

(a) Etching and exfoliation processes for Ti₃C₂ MXene. Reproduced with permission [8]. Copyright 2011, Wiley-VCH. (b) Formation of MXene alloys with varying degrees of ordering. Reproduced with permission [23]. Copyright 2017, American Chemical Society. (c) Synthesis and delamination of Mo₂C MXene. Reproduced with permission [24]. Copyright 2016, Wiley-VCH. (d) Structures of Ti₃C₂ MXene produced by different routes. Reproduced with permission [22]. Copyright 2016, Wiley-VCH.

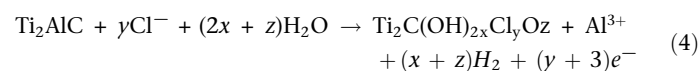
HCl or sulfuric acid (H₂SO₄) [31]. Compared with the conventional HF etching approach, MXenes obtained by the fluoride salt assisted etching method have lower fluorine content.

Molten Salt Etching. A molten fluoride salt etching method was developed by Urbankowski et al., where Ti₄N₃ can be successfully achieved by etching the Ti₄AlN₃ precursor with ternary eutectic molten fluoride salt at 550 °C under argon atmosphere (Fig. 3a) [32]. However, the as-synthesized Ti₄N₃ exhibits lower crystallinity than the MXenes obtained by the HF-etching method, indicating that there are still some intricate issues in the molten fluoride salt etching method. Very recently, a molten Lewis acidic etching approach has been revealed, where chlorine-terminated MXenes can be achieved by etching late transitional element based MAX phases [33]. This approach has been explored to various late transitional elements based MAX phases with different late transition-metal halides, such as CdCl₂, FeCl₂, CuCl₂, and AgCl [34]. As can be seen in Fig. 3b, the Ti₃SiC₂ MAX phase can react with CuCl₂ molten salt, subsequently releasing SiCl₄ gas, resulting in the formation of Ti₃C₂. In addition, the surface groups can be tuned by post-modification, giving further opportunity to explore the functionality of the MXenes [35].

Alkali Etching. In order to avoid the post-treatment of fluoride-containing waste solution, a fluoride-free etching process has been preferred in recent years. Taking advantage of the amphotericity of elemental Al, Li et al. proposed an alkali-assisted etching method to fabricate fluorine-free Ti₃C₂ by utilizing an NaOH solution as a corrosive medium [38]. As revealed, the Al hydroxides can be well dissolved at high temperature while the high alkaline concentration prevents the oxidation of the as-synthesized Ti₃C₂.

Electrochemical Etching. The electrochemical etching approach is proved to be another effective strategy for selective etching of the MAX phases. As shown in Fig. 3c, the mixture of tetramethylammonium hydroxide (TMAOH) and ammonium chloride has been used as electrolyte for electrochemical etching

of Ti₃AlC₂ phase [36]. In addition, Sun et al. successfully fabricated Ti₂CT_x flakes from the Ti₂AlC phase by an electrochemical etching method in a diluted HCl aqueous electrolyte [39]. The electrochemical reaction on the working electrode can be expressed as follows:



UV Irradiation Etching. Very recently, a novel UV-induced selective etching method was developed by etching Mo₂Ga₂C in a much milder phosphoric acid (H₃PO₄) solution [37]. As shown in Fig. 3d, fluorine-free mesoporous Mo₂C was obtained by UV irradiation and subsequent ultrasonic delamination. Hazardous and corrosive acids are hardly used in the aforementioned approaches, which enlighten the fabrication of other MXenes with more environment friendly methods.

Bottom-up strategy

In order to achieve stoichiometric control of the elemental content, a bottom-up strategy has been demonstrated for the synthesis of MXenes [40–42]. Chemical vapor deposition (CVD) approaches are commonly utilized for generating MXenes with specific terminations [43]. As revealed, Xu et al. synthesized a large area α-Mo₂C (>100 μm) using methane as carbon source and a Cu/Mo foil as substrate [40]. The size and thickness of Mo₂C can here be tuned and various shapes can be obtained by varying the experimental conditions. This approach was further improved by Jia et al., where N doped Mo₂C flakes were successfully fabricated by employing MoO₃ as Mo source and dicyandiamide as C/N source, respectively [44]. Moreover, the CVD approach can also be applied for the fabrication of MXene-based heterojunctions by utilizing traditional 2D materials as substrates. For instance, Geng et al. reported that a Mo₂C/graphene vertical heterostructure could be obtained by in-situ growth of 2D Mo₂C on graphene substrate [42]. The as-synthesized Mo₂C is free of terminations with few atomic

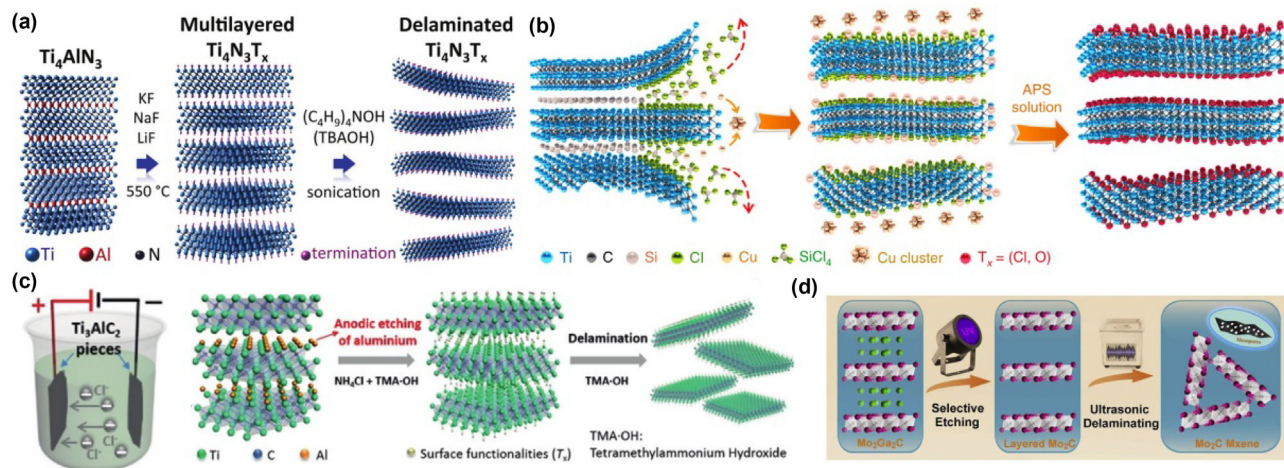


FIGURE 3

(a) Preparation of Ti_4N_3 MXene by a molten salt treatment. Reproduced with permission [32]. Copyright 2016, Royal Society of Chemistry. (b) Lewis acidic etching procedure from Ti_3SiC_2 MAX with CuCl_2 molten salt. Reproduced with permission [34]. Copyright 2020, Springer Nature. (c) Electrochemical etching process for Ti_3C_2 MXene. Reproduced with permission [36]. Copyright 2018, Wiley-VCH. (d) UV-induced selective etching for Mo_2C MXene from $\text{Mo}_2\text{Ga}_2\text{C}$ MAX. Reproduced with permission [37]. Copyright 2020, Elsevier.

defects, which is beneficial for the investigation of the intrinsic properties of the MXenes. In addition, novel 2D MXenes can be obtained by in-situ atomic layer growth. As shown in Fig. 4a, Ti_4C_3 and Ti_5C_4 can successfully be prepared by growing hexagonal TiC single adlayers on Ti_3C_2 substrate, which provides a controllable fabrication of novel MXenes with large area and high quality [45].

Moreover, salt-templated synthesis is another emerging approach especially useful for ultrathin 2D transition metal nitrides such as V_2N , W_2N , and Mn_3N_2 [46,50]. As can be seen in Fig. 4b, $\text{MnCl}_2\text{@KCl}$ can be transformed into $\text{Mn}_3\text{N}_2\text{@KCl}$ under an ammonia atmosphere due to the lattice match between KCl and Mn_3N_2 [46]. Ultrathin Mn_3N_2 flakes were obtained by washing the products with excess amount of deionized water, providing a scalable synthetic route for the 2D transition metal nitrides.

Other methods

In addition to the above-mentioned top-down and bottom-up approaches, some other methods have been used to successfully synthesize MXenes [47–49]. In 2017, Urbankowski et al. fabricated molybdenum and vanadium nitrides by ammoniation of their transition metal carbides counterparts [47]. As shown in Fig. 4c, the carbon atoms in Mo_2C and V_2C can be replaced by N elements under an ammonia atmosphere at high temperature. This approach not only opens a new avenue in the synthesis of transition metal nitrides, but also provides a nitrogen-doping method for MXenes. Jeon et al. developed another elemental transformation method to fabricate Mo_2C flakes from MoS_2 by thermal annealing [48]. As shown in Fig. 4d, CH_4 was used as C source and an atomically sharp $\text{Mo}_2\text{C}/\text{MoS}_2$ hybrid structure can be observed when partial Mo_2C is formed. As the thermal annealing time increases, MoS_2 can fully convert to Mo_2C . Lin et al. demonstrated a synthetic route for hexagon Mo_2C by the reduction of H_2MoO_5 and a corresponding carburization of MoO_3 on an amorphous carbon substrate [49]. As revealed,

MoC with a face-centered cubic structure was produced with the presence of sucrose while hexagonal closed packed Mo_2C formed on the relatively stable amorphous carbon film (Fig. 4e). This can be ascribed to the relatively inert amorphous carbon from the carbon film, which makes it difficult for carbon atoms to occupy interstitial sites. Table 1 summarizes the parameters for the synthesis of MXenes by various methods, including also the obtained morphologies.

With the rapid development of synthetic strategies, more than 30 kinds of MXenes have been fabricated. The fluoride-containing etching protocol is still a widely used strategy for most of the MXenes [52]. It should be noted that one approach might be applicable for a certain MXene but not suitable for another. Therefore, the chemical and physical properties may vary as the synthetic routes as changed, mainly due to the various surface terminations and lateral dimensions. Although there are many different protocols for fabricating MXenes, more efforts are required for modifying current approaches as well as developing novel methods, which will be helpful to synthesize MXenes with high quality and boost their further applications in various fields.

Properties of MXenes

Owing to their particular atomic structures and morphologies, MXenes exhibit unique properties that facilitate their applications in various fields. The electric, optical and mechanical properties that are essential for the photo-response properties of MXene-based photodetectors, which are mainly summarized in this section.

Electric properties

The electric properties of MXenes are in general essential for their further applications in various fields, especially for photodetection [53–55]. Due to the transition metal elements in the outer layer, bare MXenes are predicted to be metallic and possess high electron density near the Fermi level [56]. Compared with the

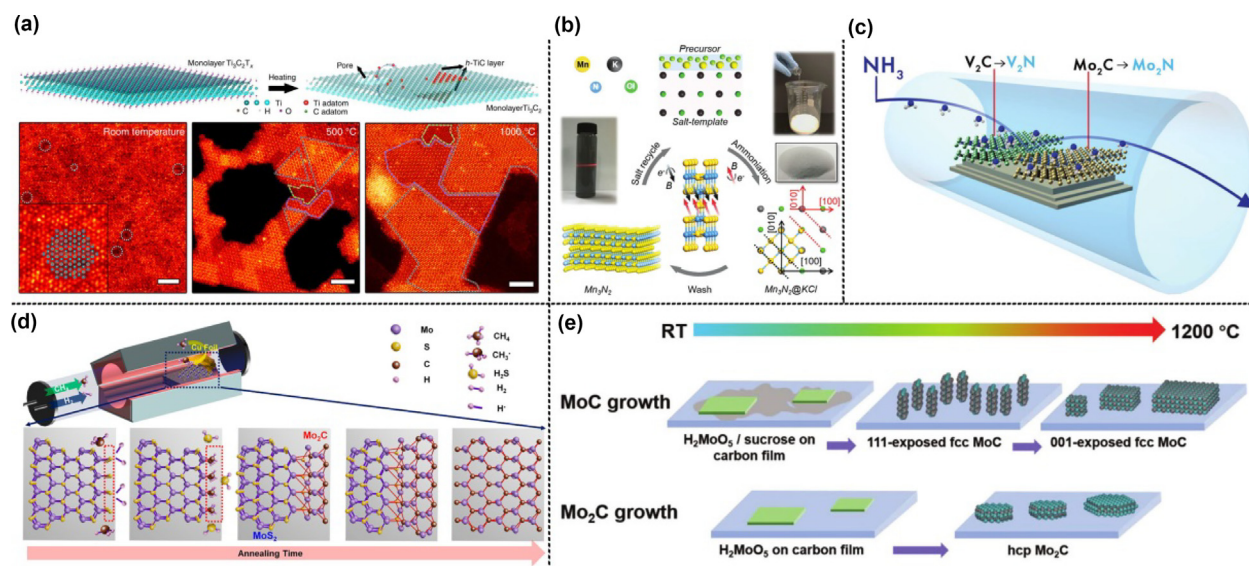


FIGURE 4

(a) Homoepitaxial growth of h-TiC on Ti_3C_2 substrate and the resultant STEM images. Reproduced with permission [45]. Copyright 2018, Springer Nature. (b) Synthetic route of Mn_3N_2 MXene by a salt-templated approach. Reproduced with permission [46]. Copyright 2019, Wiley-VCH. (c) Synthesis of nitride MXenes from carbide MXenes by gas treatment strategy. Reproduced with permission [47]. Copyright 2017, Royal Society of Chemistry. (d) Schematic illustration for the synthesis of Mo_2C MXene by thermal annealing approach. Reproduced with permission [48]. Copyright 2018, American Chemical Society. (e) Reaction growth of MoC and Mo_2C on carbon film. Reproduced with permission [49]. Copyright 2017, Wiley-VCH.

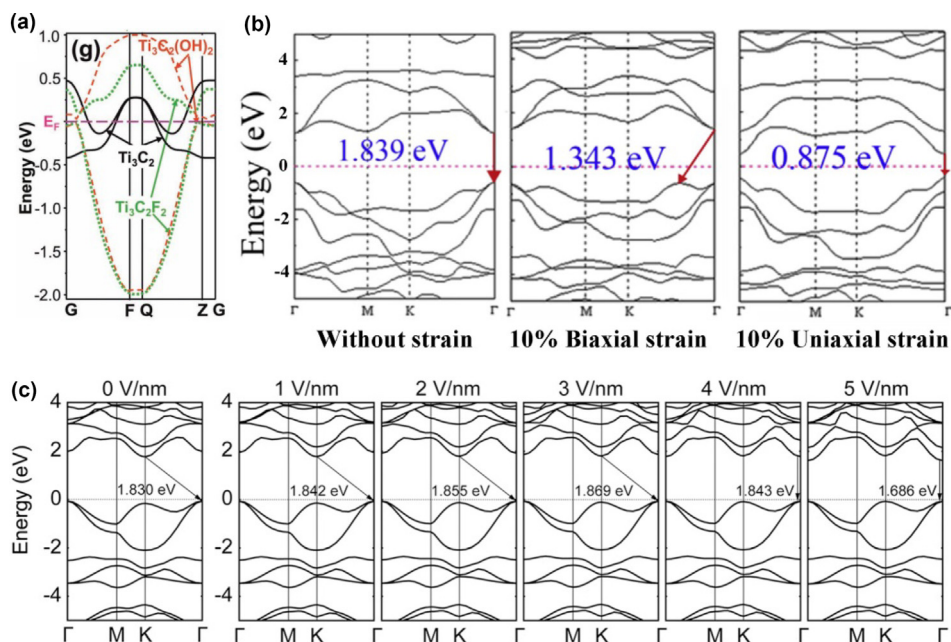
TABLE 1

Parameters and morphologies for the synthesized MXene with different methods.

Methods	Materials	Precursors	Condition	Size	Thickness	Termination	Ref.
HF Etching	Nb_2CT_x	Nb_2AlC	40% HF, R.T., 24 h	48–255 nm	2.4–3.0 nm	–F, –OH	[51]
Modified Acid Etching	$\text{Ti}_3\text{C}_2\text{T}_x$	Ti_3AlC_2	$\text{LiF}:\text{HCl}$ (7.5:23.4) 35 °C, 24 h	4–15 μm	2.7 nm	–OH, –F, –O	[22]
Molten Salt Etching	$\text{Ti}_3\text{C}_2\text{T}_x$	Ti_3SiC_2	CuCl_2 , 750 °C, 24 h	–	Multi-layer	–Cl, –O	[34]
Alkali Etching	$\text{Ti}_3\text{C}_2\text{T}_x$	Ti_3AlC_2	27.5 M NaOH, 270 °C, 12 h	–	Multi-layer	–OH, –O	[38]
Electrochemical Etching	$\text{Ti}_3\text{C}_2\text{T}_x$	Ti_3AlC_2	1.0 M NH_4Cl and 0.2 M TMAOH, 5 V, R.T., 5 h	> 2 μm	1.2 nm	–O, –OH	[36]
UV Irradiation Etching	Mo_2CT_x	$\text{Mo}_2\text{Ga}_2\text{C}$	85% H_3PO_4 , UV light irradiation (100 W), R.T., 3–5 h	> 1 μm	6 nm	–O	[37]
CVD	$\alpha\text{-Mo}_2\text{C}$	CH_4 , Mo foil	1085 °C under H_2 , 2–50 min	> 100 μm	6.7–11.2 nm	–	[40]
Salt-Templated	Mn_3N_2	MnCl_2 , KCl, NH_3	750 °C for 7 h	> 1 μm	1.37–4.24 nm	–	[46]
Ammoniation	V_2NT_x	V_2CT_x , NH_3	600 °C for 1 h	–	2–20 μm	–O	[47]
Thermal Annealing	Mo_2C	MoS_2 , CH_4 , H_2	820 °C over 4 h	100 μm	3–100 nm	–	[48]

inner transition metal layers, the outer ones are suggested to be more important as their surface terminations can greatly alter the electronic band structures of the MXenes. As the first member in the MXene family, bare Ti_3C_2 is metal-like with zero bandgap while the bandgaps of $\text{Ti}_3\text{C}_2(\text{OH})_2$ and $\text{Ti}_3\text{C}_2\text{F}_2$ are calculated to be 0.05 and 0.1 eV, respectively (Fig. 5a) [8]. This can be attributed to the formation of a new energy band near the Fermi surface due to the electron transfer from the transition metal atoms to the terminations. In addition, the orientation and co-existence of surface terminations also influence the electric properties of the MXenes. For example, the calculated band gap of $\text{Cr}_2\text{CF}(\text{OH})$ is about 0.383 eV, which is similar to that of $\text{Cr}_2\text{C}(\text{OH})_2$ (0.396 eV) while it is significantly lower than that of $\text{Cr}_2\text{-CF}_2$ (1.105 eV) [57].

Generally, the transition metal atoms play an important role in influencing the electric properties of MXenes [60]. Most of the surface-terminated MXenes have indirect band gaps with energy ranging from 0.25 to 2.0 eV, except for $\text{Sc}_2\text{C}(\text{OH})_2$ which has a direct band gap [61,62]. In addition, different X elements give rise to dissimilar band structures, where the additional electrons in the N atom endow a stronger metallic property. Apart from the chemical composition and surface terminations, the band structure of MXenes can also be tuned by external strain and by electric fields [63–65]. For instance, the band gap of ScNbCO_2 reduces from 1.839 eV to 1.343 eV and 0.875 eV under the biaxial strain and uniaxial strain of 10%, respectively (Fig. 5b) [58]. As revealed by Li et al., the bandgap rapidly decreases as the increment of the interlayer electric field and an indirect-to-direct

**FIGURE 5**

Bandgap structure of MXenes under various conditions. (a) Calculated band structure of single-layer Ti_3C_2 with various terminations. Reproduced with permission [8]. Copyright 2011, Wiley-VCH. (b) The band gap of ScNbCO_2 under external strain. Reproduced with permission [58]. Copyright 2017, Elsevier. (c) The band gap of Sc_2CO_2 under external electric fields. Reproduced with permission [59]. Copyright 2014, Royal Society of Chemistry.

band structure transition is observed under 3.7 V/nm (Fig. 5c) [59].

The coherent transport calculations have revealed that metallic MXenes are highly conductive and that the electric conductivity is significantly anisotropic along various lattice directions [66–68]. This can be mainly ascribed to the effective mass ratio between electrons and holes, where the ratio is rather small in the basal plane and estimated to be infinite perpendicular to the layers [69]. Owing to the highly anisotropic band structure and smaller energy dispersion along the c direction, the conductivity of $\text{Ti}_3\text{C}_2\text{T}_x$ decreases with the increasing layer number of the MXene. As summarized by Hantanasirisakul et al., the room-temperature conductivity of MXenes ranges from less than 1 S/cm to thousands S/cm, and shows a strong relationship with the synthetic strategy and sampling process [61]. Surface terminations also show considerable impact on the electron transport by changing the electronic states and electrostatic profile, where the resistance of $\text{Ti}_3\text{C}_2\text{F}_2$ is estimated to be four times lower than that of pristine Ti_3C_2 [70]. Moreover, the conductivity of Ti_3C_2 increases from 850 to 2410 S/cm by annealing at 600 °C, which can be attributed to the decreased surface functionalities [71]. These outstanding electric properties of MXenes are here confirmed by both theoretical calculations and experimental investigations, something that facilitate their potential applications in various fields.

Optical properties

Generally, the optical properties of MXenes can be divided into two main components, namely linear and nonlinear optical properties [61]. A large amount of effort has been made to unravel the linear optical properties of various MXenes, including transmittance, absorption, reflection, and photoluminescence.

It has been revealed that the transmittance of MXene films increases with the decrement of thickness [72]. For instance, the transmittance is higher than 90% for a 2.5 nm thick $\text{Ti}_3\text{C}_2\text{T}_x$ film while it is lower than 15% as the thickness increases to 73 nm. Fig. 6a depicts UV–vis spectra of Nb_2C nanosheets under various concentrations where a broad and strong absorption band is observed ranging from 400 to 1350 nm. In addition, the elemental doping of MXenes changes both the absorption peak and intensity. As revealed by Guo et al., there are two main peaks that show up in ScNbCO_2 (peak value of 369 and 621 nm) with a calculated absorption area between 300 and 1000 nm, which are about 20 times larger than that of Sc_2CO_2 (Fig. 6b) [58]. As revealed by Lu et al., the size dimension also affects the transmittance of this MXene, where Ti_3C_2 quantum dots (QDs) show two unique transmission bands at 1500 and 2900 cm^{-1} in the measured Fourier transform infrared spectra due to the quantum confinement effect (Fig. 6c) [74]. The quantum confinement also endows MXenes excellent photoluminescence properties, and a high quantum yield can be achieved (Fig. 6d) [75].

The surface terminations and intercalations have shown remarkable influence on the optical properties of MXenes [78–80]. As revealed by Berdiyrov et al., pristine and –O terminated Ti_3C_2 exhibit larger in-plane absorption coefficients than the –F and –OH terminated ones, indicating a tunable application of these MXenes as transparent electrodes [79]. Fig. 6e displays the change of transmittance of $\text{Ti}_3\text{C}_2\text{T}_x$ thin films with various chemical intercalations [76]. Compared with the 74.9% transmittance of pristine films, tetramethylammonium hydroxide intercalated $\text{Ti}_3\text{C}_2\text{T}_x$ exhibits the biggest change of 17.1% while the intercalation of other inorganic bases also increases the transmittance.

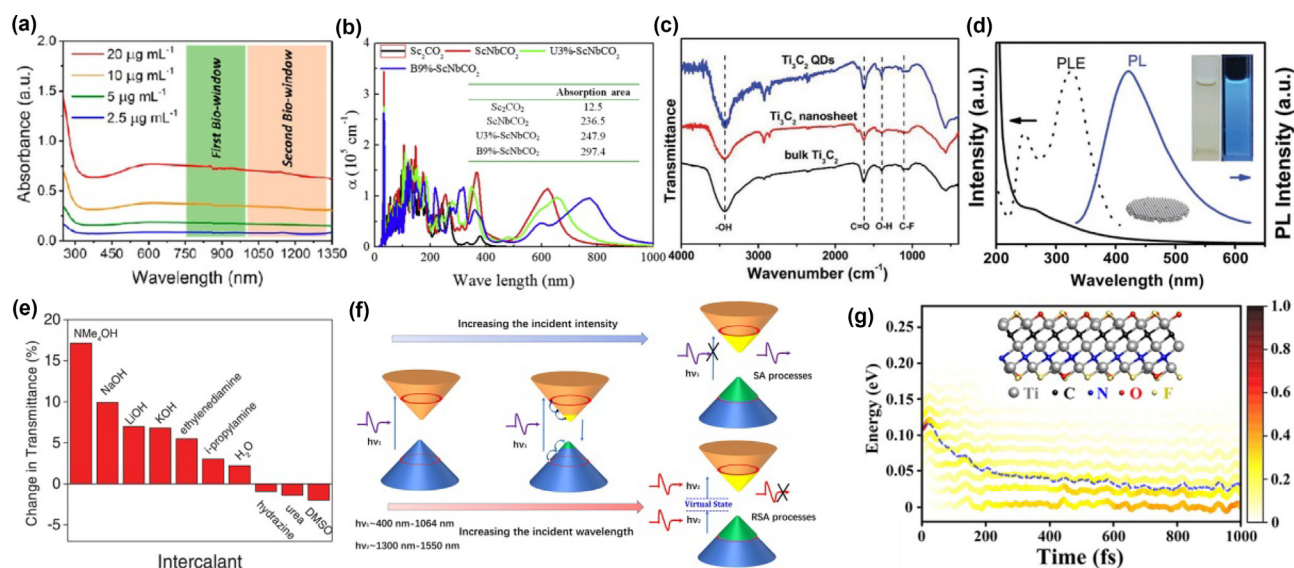


FIGURE 6

Optical properties of MXenes. (a) Vis–NIR absorbance spectra of Nb₂C under various concentrations. Reproduced with permission [73]. Copyright 2017, American Chemical Society. (b) Absorption coefficient of Sc₂CO₂ and ScNbCO₂ under external strain. Reproduced with permission [58]. Copyright 2017, Elsevier. (c) FTIR spectra of bulk Ti₃C₂, Ti₃C₂ nanosheets, and Ti₃C₂ QDs. Reproduced with permission [74]. Copyright 2019, Wiley-VCH. (d) UV–vis, PLE, and PL spectra of Ti₃C₂ QDs. Reproduced with permission [75]. Copyright 2017, Wiley-VCH. (e) Change in transmittance of the films with various intercalations. Reproduced with permission [76]. Copyright 2016, Wiley-VCH. (f) The schematic illustration of saturable absorption and reverse-saturable absorption of Nb₂C nanosheets. Reproduced with permission [51]. Copyright 2020, Wiley-VCH. (g) Time-dependent electron energy change at 300 K for Ti₃CN MXene. Reproduced with permission [77]. Copyright 2022, American Chemical Society.

Nonlinear optics focuses on the interaction between light and matter where the materials are generally irradiated by intense light [81–83]. Very recently, Gao et al. revealed both saturable absorption and reverse-saturable absorption of Nb₂C nanosheets, which stem from the one-photon absorption and multi-photon absorption, respectively [51]. Moreover, the relaxation dynamics of Nb₂C has been systematically investigated by means of transient absorption spectroscopy and a lateral size effect has been illustrated by a phonon-bottleneck mechanism (Fig. 6f). In addition, the hot electron relaxation process has been theoretically investigated via nonadiabatic molecular dynamic calculations (Fig. 6g) [77]. As revealed, the photo-generated carriers quickly convert into hot carriers with a Fermi-Dirac distribution and cooled down by fast relaxation through electron–electron and electron–phonon scattering in the conduction band. These are results that indicate that MXenes are promising materials for broadband ultrafast photonics and optoelectronic devices, holding the potential for breakthrough developments in these fields.

Collectively, the linear and nonlinear optical properties of MXenes favor their further applications in various fields. Compared with the thoroughly investigated linear properties of MXenes, the understanding of their nonlinear properties is still at the infancy stage and their light-matter interactions require further exploration. Therefore, more efforts are needed to reveal the nonlinear optical properties of various MXenes before their practical applications can be implemented.

Mechanical properties

The intrinsic mechanical properties of bare Ti_{n+1}C_n (*n* = 1, 2, or 3) have been systemically investigated by molecular dynamics simulations, where the thickness dependence also has been studied

[84]. Quite astonishing, there is no obvious correlation between the Young's modulus and the atomic layers of Ti_{n+1}C_n, where the in-plane Young's modulus is calculated to be 597, 502, and 534 GPa as the number of carbon layers increases from 1 to 3 (Fig. 7a). Due to the stretching of Ti–C bonds, Ti₂C could sustain a strain of 18% under biaxial tension [85]. The strain of Ti₂C reaches 28% after surface modification of oxygen, which can be attributed to the significant charge transfer from the Ti–C bonds to the Ti–O ones (Fig. 7b). Besides, the surface terminations also enhance the mechanical properties of stacked MXene films and their interlayer interactions are remarkably higher than that of graphene [87,88]. Owing to the formation of hydrogen bonds, the –OH terminated MXenes show the smallest interlayer distance and the highest interlayer coupling among MXenes with various terminations. The breaking strengths of the various MXenes are predicted to be in the range from 92 to 161 N/m, implying excellent mechanical properties [89]. However, there might be some defects in the as-synthesized MXenes, making the mechanical properties a bit inferior compared to those obtained by theoretical calculations. As revealed by Ling et al., a Ti₃C₂T_x film with a thickness of 5.1 μm can support 4000 times of its own weight, which can be further enhanced by introducing additives such as chitosan and polyvinyl alcohol [90]. Recently, the rheological properties of MXenes have been investigated as motivated by that MXene inks can be directly used to fabricate various devices [91]. As revealed by Akuzum, an apparent shear-thinning behavior can be observed in both single-layer and multi-layer MXene dispersions, while the viscosity increased with the increment of Ti₃C₂T_x concentration [86]. It is well known that different processes require various rheological properties of dispersions, for instance, spray coating requires high vis-

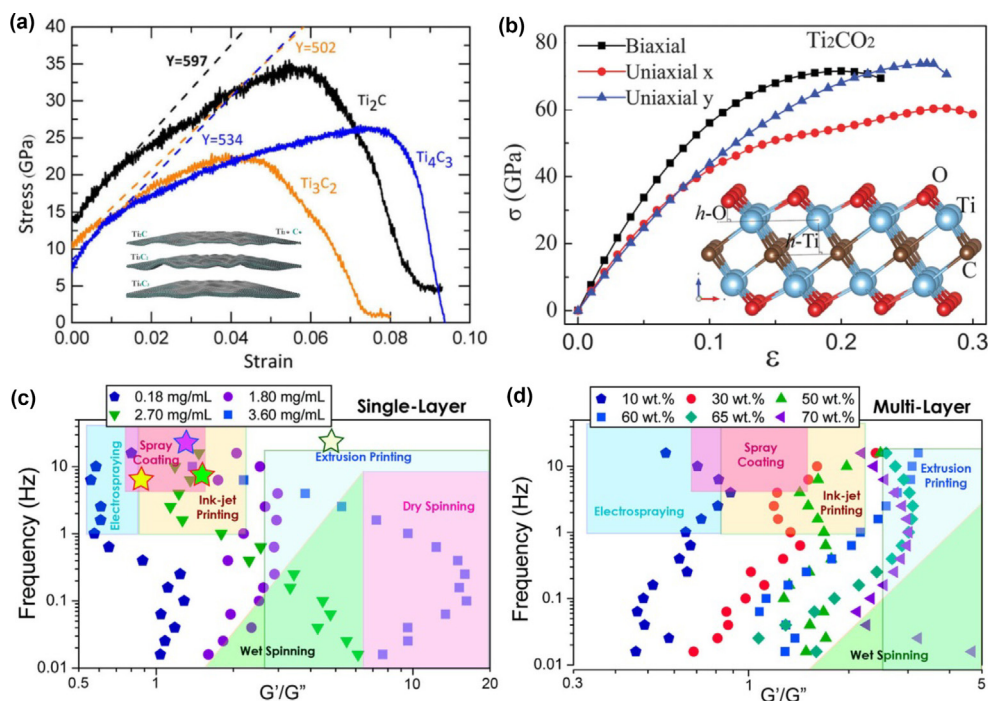


FIGURE 7

Mechanical properties of MXenes. (a) Simulated mechanical properties of $Ti_{n+1}C_n$ ($n = 1, 2, \text{ and } 3$). Reproduced with permission [84]. Copyright 2015, IOP Publishing Ltd. (b) Calculated stress-strain curves of Ti_2CO_2 . Reproduced with permission [85]. Copyright 2015, Royal Society of Chemistry. (c) Frequency dependency of the G'/G'' for single-layer $Ti_3C_2T_x$. (d) Frequency dependency of the G'/G'' for multi-layer $Ti_3C_2T_x$. Reproduced with permission [86]. Copyright 2018, American Chemical Society.

cous modules while extrusion printing needs high elastic modules. As shown in Fig. 7c and d, single-layer and multi-layer MXenes show distinct rheological behavior, which provide various printing possibilities, including ink writing, patterned coating, inkjet and 3D printing.

Considering results of theoretical simulations as well as experimental investigations, MXenes have been revealed to possess various properties which can be tuned by intrinsic compositions and post-treatments. Their potential applications in different fields have been demonstrated, including energy storage devices [92], biomedicine [93], EMI shieldings [94], catalysts [54], photodetectors [20], and other fields [95]. The property control of various MXenes is ever improving, something that certainly can further enhance the performance of MXene-based devices.

MXene-based Photodetectors

Taking advantage of the unique photoelectrical properties, MXenes are proved to be excellent building blocks for high-performance photodetectors with various structures [19,20]. For traditional FET-type photodetectors, metal electrodes should be deposited on the substrate *via* standard photolithography and electron-beam evaporation, where the individual MXene flake is subsequently moved onto the metal electrodes by a physical transfer approach [22]. In order to simplify the procedure, drop-casting, spray-coating, or spin-coating strategies can be used to deposit multiple flakes of the MXene onto the metal electrode, where the photo-response performance of the multi-layer MXene then is detected and the influence of thickness can so be explored [91]. In addition, large-scale flexible photodetectors can

be achieved by vacuum filtration or by coating the MXene (also MXene composites) on flexible substrates [96,97]. When the MXene is used to substitute the metal electrode, a pre-designed mask is used to control the position and size of the MXene-electrode, where the active materials can be either under the mask or be subsequently transferred on to the MXene-electrode [98]. Recently, several novel structures have also been designed for MXene-based photodetectors. For instance, Lim et al. applied a one-way continuous deposition strategy to fabricate a sandwich structural capacitive photodetector [99]. Zhang et al. prepared an MXene-based working electrode by spin-coating an MXene slurry onto flexible ITO-coated PET substrates, where a standard three electrode PEC-type photodetection system was established to reveal the photo-response performance [100]. As mentioned, MXenes can be utilized as electrodes due to their excellent conductivity, replacing the traditional metal electrodes. On the other hand, MXenes themselves have been extended as active materials owing to their tunable work function and band structure, including pristine MXenes and MXene-based composites.

Electrode

Benefiting from the high conductivity, MXene there have been attempts to replace the traditional metal electrodes when building photodetectors [101–103]. In 2016, Mariano et al. demonstrated that solution processed $Ti_3C_2T_x$ films exhibited a low resistances of 437 Ω/sq , where the metallic nature was further confirmed by field effect transistor measurements [104]. Combining the high transmittance, MXene films show here great

potential for the next generation of transparent conductive electrodes. Xu et al. reported an electrode application of $\text{Ti}_2\text{C}(\text{OH})_{x\text{F}_y}$ in field effect transistor (FET) type photodetectors based on WSe_2 and MoS_2 active materials [105]. A pinning effect was found at the $\text{MoS}_2/\text{Ti}_2\text{C}(\text{OH})_{x\text{F}_y}$ interface due to the relatively low electron barrier between MoS_2 and $\text{Ti}_2\text{C}(\text{OH})_{x\text{F}_y}$. In addition, a complementary metal–oxide semiconductor inverter was successfully fabricated based on the $\text{Ti}_2\text{C}(\text{OH})_{x\text{F}_y}$ electrode, where WSe_2 and MoS_2 were assigned as n- and p-channels, respectively.

The introduction of MXene electrodes has further endowed photodetector unique properties [106–108]. For instance, Kang et al. fabricated a vertical van der Waals heterostructures combining $\text{Ti}_3\text{C}_2\text{T}_x$ and n-type silicon where the as-prepared photodetector exhibited self-driven performance with high response and recovery speed [109]. They also constructed a self-powered two-sided photodetector based on Mo_2C -graphene and fluorine-doped tin oxide (FTO) electrodes [110]. Owing to the high transparencies of Mo_2C MXene and FTO, the photodetectors could respond to light from both sides. In addition, the high transparency of the MXene electrode the transport of light with various wavelengths was facilitated, which maintains the broadband response of the active materials [111]. As can be seen in Fig. 8a, a highly sensitive and broad-spectral response photodetector was fabricated based on $\text{Mo}_2\text{C}/\text{MoS}_2$ hybrid structure with multiple Mo_2C periods (400–1000 nm). Compared with the MoS_2 -based photodetector, the on/off ratio of $\text{Mo}_2\text{C}/\text{MoS}_2$ hybrid structure is enhanced by three orders of magnitude (Fig. 8b), which can be ascribed to the surface plasmons of metallic Mo_2C upon illumination and subsequent hot carrier injection to MoS_2 . Moreover, the peak photoresponse can be controlled by adjusting the grating period of Mo_2C since the grating period is closely related to the incident light wavelength. As shown in Fig. 8c, a broad spectral range detection (405–1310 nm) can be achieved *via* integrating the grating periods, where high sensitivity and on–off ratio are remained. Yang et al. further confirmed the performance enhancement of a stripe-shape photodetector, where a plasmonic InSe-based avalanche material was fabricated (Fig. 8d) [112]. By patterning Ti_2CT_x into nanoribbon arrays, the performance of the InSe/ Ti_2CT_x photodetector could be greatly enhanced, which can be ascribed to the improved light absorption and avalanche carrier multiplication effect.

The advantages of replacing metal by MXene are not only the low processing cost, but also the enhanced performance [114–116]. As can be seen in Fig. 8e, a $\text{Ti}_3\text{C}_2\text{T}_x$ -GaAs- $\text{Ti}_3\text{C}_2\text{T}_x$ (MX-S-MX) photodetector was fabricated by mask set and lithography technique [98]. Compared with the traditional metal electrode based Ti/Au-GaAs-Ti/Au (MSM) photodetector, the MX-S-MX device shows higher photocurrent, external quantum efficiency (EQE), and responsivity. A similar phenomenon was also observed by Yin et al., where the larger photocurrent compared with Au contacts is attributed to the larger photo-responsive active areas of the MXene conductive films and the plasmon-assisted hot carriers [117]. Recently, Hu et al. also compared the photoresponse performance of organic photosensitive materials (RAN) based on MXene and Au electrodes (Fig. 8f). Fig. 8g shows the working mechanism of organic–inorganic $\text{Ti}_3\text{C}_2\text{T}_x$ -RAN heterojunctions, where a Schottky junction is formed

between MXene and a RAN film. Considering the work function of 4.8 eV, with the MXene electrode it is easier to inject carriers into RAN than using a traditional Au electrode. In addition, the electronegative N and O atoms in RAN could form hydrogen bonds with MXene, which further enhances the synergistic effect. As can be seen in Fig. 8h, the on–off ratio of the $\text{Ti}_3\text{C}_2\text{T}_x$ -RAN device is much higher than that of Au-RAN. Moreover, the $\text{Ti}_3\text{C}_2\text{T}_x$ -RAN array can be used for accurate image sensing and building laser power intensity monitor systems, so further extending the applications of MXene-based photodetectors.

It is well-known that 2D MXenes can be easily deposited on various substrates, which offers a high flexibility of the resultant devices. Deng et al. demonstrated large-area photodetector arrays by spraying conductive $\text{Ti}_3\text{C}_2\text{T}_x$ MXene and 2D CsPbBr_3 on common paper (Fig. 9a) [118]. Owing to the matched work function between MXene and the perovskite crystal, the photodetector shows fast separation and efficient extraction of carriers, which contributes to the fast response speed (~ 18 ms) and high on/off ratio ($\sim 2.3 \times 10^3$). In addition, the as-prepared device exhibits excellent flexibility and stability after 1500 times bending, where apparent on–off signals are observed and 85% of its initial photocurrent is remained (Fig. 9b). Considering the economic preparation of an all-sprayed-processable method, 2D MXene-based flexible photodetectors show great potential for wearable optoelectronic devices and photocommunication.

Inspired by leaf vein networks, Chen et al. proposed a transparent flexible electrode based on facile coating of $\text{Ti}_3\text{C}_2\text{T}_x$ MXene [97]. As revealed, the resultant electrodes exhibit many advantages, such as superior optical transmittance, outstanding flexibility, dependable mechanical strength, being freestanding and lightweight. Taking advantage of the tunable work function of MXenes, the MXene-based electrodes could match different photodetectors with high flexibility and performance. Very recently, MXene-based electrodes were utilized to optimize p- CsCu_2I_3 /n- $\text{Ca}_2\text{Nb}_{3-x}\text{Ta}_x\text{O}_{10}$ junction photodetectors *via* tuning the work function [119]. The schematic diagram of devices and energy band structures in thermal equilibrium state are illustrated in Fig. 9c. As revealed, the effect of lowering the dark current under reverse bias will be more significant at lower work function. Therefore, the photodetector based on a polyethyleneimine ethoxylated modified MXene electrode (~ 4.55 eV) exhibits the best rectification ratio (1.6×10^4) and responsivity (~ 81.3 A/W) values, which are much higher than those based on traditional Au or pristine MXene electrodes. Moreover, the as-prepared large-scale flexible UV detectors maintain 80% of the original photocurrent after 5000 bending cycles, which also shows potential applications in image sensing and optoelectronic logic gates.

In addition to traditional FET-type photodetectors, MXene-based electrodes can also be utilized to build other novel photodetectors. For instance, Lim et al. demonstrated a flexible capacitive photodetector based on two layers of opposing transparent MXene electrodes [99]. As shown in Fig. 9d, a one-way continuous deposition technology was applied for the construction of the photodetector, where MXene nanosheets were deposited on both sides of a ZnS:Cu/poly(vinyl butyral) (PVB) film. PVB was used to disperse the active ZnS:Cu particles, which also

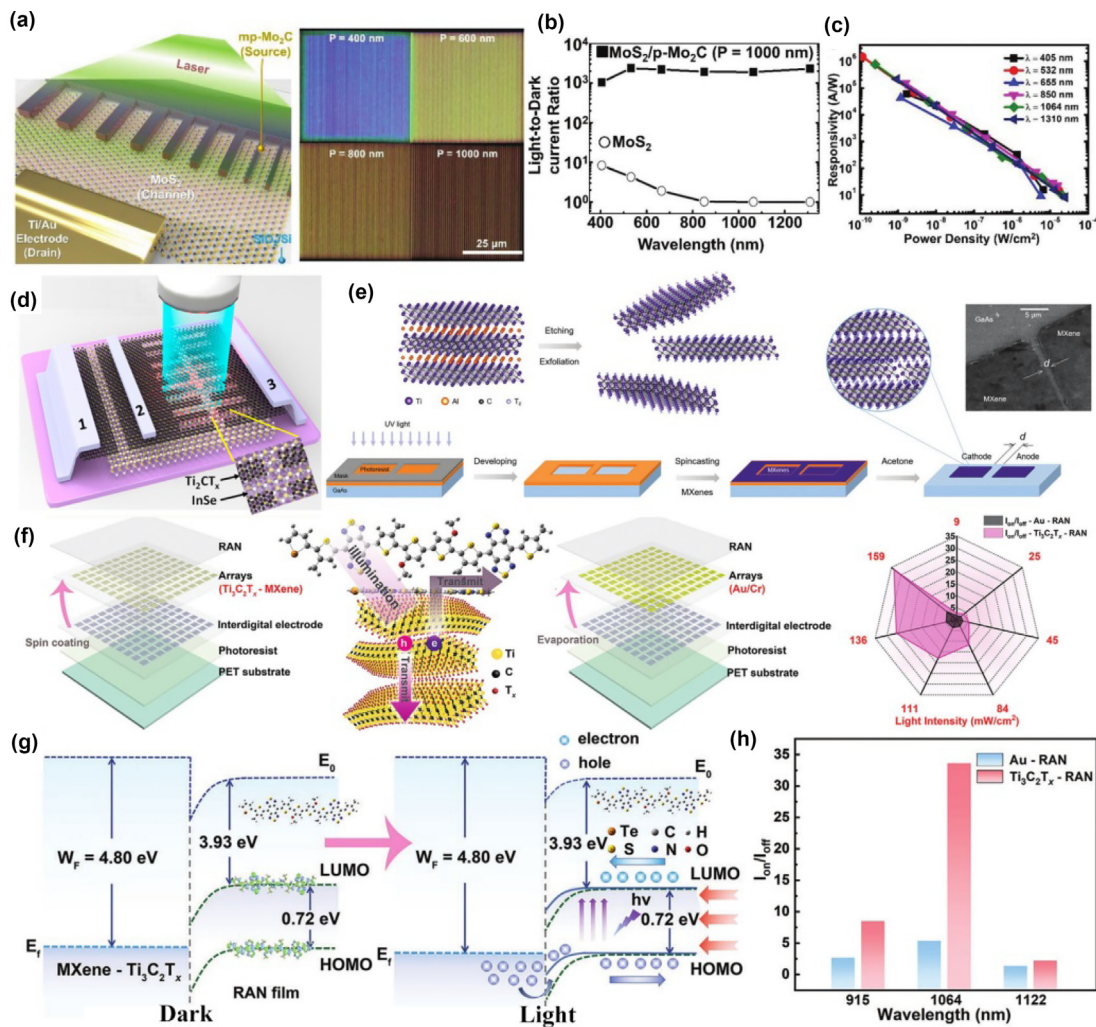


FIGURE 8

(a) Schematic illustration of MoS₂/Mo₂C based photodetector with multiple Mo₂C periods. (b) Wavelength dependence of the on/off ratios for the MoS₂/Mo₂C hybrid device with 1000 nm Mo₂C periods and pristine MoS₂ device. (c) Responsivity of the MoS₂/Mo₂C hybrid device against light power density under the illumination of different wavelengths. Reproduced with permission [111]. Copyright 2019, Wiley-VCH. (d) Structures of unpatterned and patterned InSe/Ti₃CT_x photodetectors. Reproduced with permission [112]. Copyright 2019, American Chemical Society. (e) Fabrication process of Ti₃C₂T_x-GaAs-Ti₃C₂T_x photodetector device. Reproduced with permission [98]. Copyright 2019, Wiley-VCH. (f) Structure diagram of Ti₃C₂T_x-RAN and Au-RAN photodetectors with the compared on-off ratios. (g) Energy band diagram of Ti₃C₂T_x-RAN under dark and light. (h) Tested on/off ratios under different light wavelengths of 915, 1064, and 1122 nm. Reproduced with permission [113]. Copyright 2022, Wiley-VCH.

served as a free-standing binder between the active materials and the MXenes. As revealed, high photo-capacitance (2 nF) and photosensitivity (12.5 μF/W) was achieved while a fast response of 0.034/0.751 s were observed, which is about 2 orders of magnitude better than for reported capacitive photodetectors. The enhanced photoresponse performance can be ascribed to the high conducting coverage of the two MXene electrodes as well as to the high ZnS:Cu density in the matrix. In addition, the as-fabricated device exhibits excellent mechanical stability owing to a synergistic effect between the PVB polymer and the MXenes. The capacitance remains almost unchanged after bend testing for 1000 cycles with a bending radius of 2 mm. Moreover, the photoresponse properties were maintained when a part of the device is cut off (Fig. 9e), which can be attributed to the excellent solid bonding between the composite active materials and the MXene electrodes.

Active Materials

MXene composites

MXene composites can serve as the active materials in the photodetectors, something that been widely investigated in recent years. Table 2 summarizes the detailed parameters for MXene-based photodetectors where MXene composites serve as the active materials, including the device structure, bias voltage, and detected wavelength. The corresponding photo-response performance is also included, such as photocurrent density, photoresponsivity, response time, and detectivity.

Generally, the oxidation of active materials can induce an undesirable degradation and further cause penalty for the device performance, especially for the long-term stability. Hence, there has been a strive to suppress the oxidation process by several strategies including chemical and physical encapsulation [138]. However, the MXenes are unavoidably in contact with air during

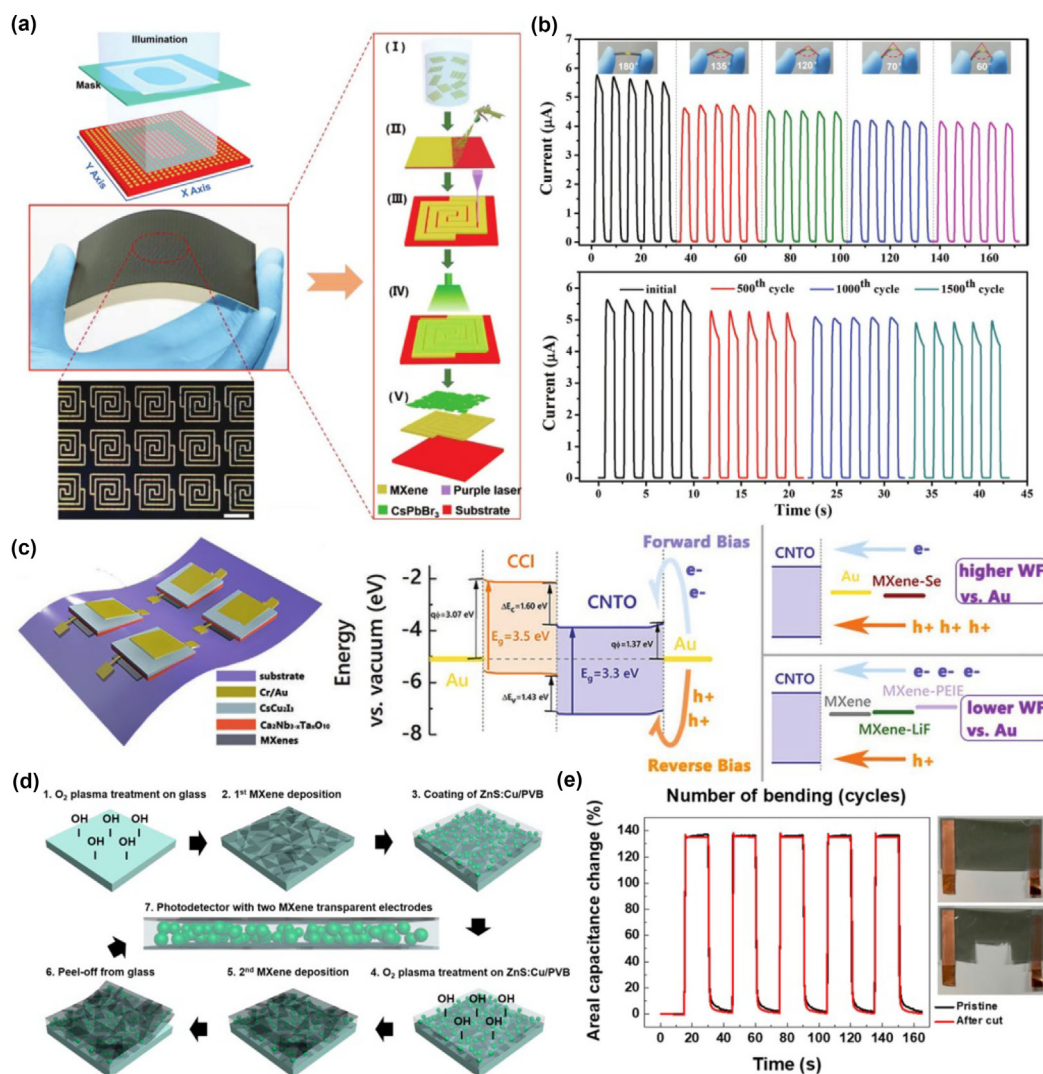


FIGURE 9

(a) Fabrication of large-area array photodetector based on conductive $\text{Ti}_3\text{C}_2\text{T}_x$ MXene and 2D CsPbBr_3 . (b) Flexibility and stability test of the large-area array photodetector. Reproduced with permission [118]. Copyright 2019, Wiley-VCH. (c) Structural illustration and energy band diagram of Au/p- Cu_2Te /n- $\text{Ca}_2\text{Nb}_{3-x}\text{Ta}_x\text{O}_{10}$ /MXene photodetector. Reproduced with permission [119]. Copyright 2022, Wiley-VCH. (d) One-way continuous deposition strategy for the preparation of MXene-based flexible capacitive photodetector. (e) Photo-response performances of pristine and cut photodetectors. Reproduced with permission [99]. Copyright 2021, American Chemical Society.

the preparation or post-modification, and most of the device fabrications take place under ambient conditions [139–141]. As revealed, the color of MXene colloid changes after long-time storage, indicating an air-induced oxidation in solution. SEM results also confirm the formation of titanium oxide (TiO_2) nanoparticles on un-delaminated MXenes which are stored at ambient environments [142]. Fortunately, a new strategy by controlling the oxidation process of MXenes has been investigated by several groups, which overturns the aforementioned oxidation disadvantage and further improves the device performances [124,134,143]. In 2018, Chertopalov et al. demonstrated that partially oxidized Ti_3C_2 MXene thin films exhibit obvious photoresponse in the UV region (Fig. 10a) [143]. As shown in Fig. 10b, the electrical resistance of $\text{Ti}_3\text{C}_2\text{T}_x$ dramatically changes under the irradiation of UV light, resulting in an apparent variation of the photocurrent. Compared with the ultra-long relax-

ation time of photoexcited carriers under argon atmosphere, the relaxation process can be greatly accelerated in air condition due to the spontaneous oxidation of Ti_3C_2 flakes (Fig. 10c). Considering the reversible and reproducible photoresponse, Ti_3C_2 - TiO_2 composites show potential for UV light detection, while the practical performances are far from satisfactory such as the response speed (Fig. 10d). Therefore, more efforts are needed to determine the predominant working mechanism.

In 2021, Ma et al. constructed a self-powered PEC-type photodetector based on $\text{Ti}_3\text{C}_2\text{T}_x/\text{TiO}_2$ heterojunctions, which was spontaneously oxidized from $\text{Ti}_3\text{C}_2\text{T}_x$ MXene [124]. The in-situ formed $\text{Ti}_3\text{C}_2\text{T}_x/\text{TiO}_2$ served as active materials in the two-electrode PEC photodetector, where the carriers are generated in the TiO_2 semiconductor and their transfer are promoted by the conductive $\text{Ti}_3\text{C}_2\text{T}_x$. As demonstrated, a high responsivity of 2.06 mA/W and a fast response (45 and 69 ms for rise and

TABLE 2

Compared photo-response performance of MXenes composites as active materials.

Materials	Structure	Voltage (V)	λ^a (nm)	P_{ph}^d ($\mu A/cm^2$)	R_{ph}^e (A/W)	t_{res}/t_{rec}^f (s)	D^{*g} (Jones)	Ref.
Zn ₂ GeO ₄ /Ti ₃ C ₂	PEC	6.0	254	2.9×10^1	2.0×10^{-2}	0.06/0.39	–	[120]
ZnO/Ti ₃ C ₂	FET	5.0	365	4.9×10^2	7.0	1.6/4.0	–	[121]
MAPbI ₃ /Ti ₃ C ₂ T _x	FET	2.0	525	3.4×10^2	1.7	0.019/0.066	7×10^{11}	[122]
ZnO QDs/Ti ₃ C ₂ T _x	FET	10.0	350	7.3×10^2	4.3×10^{-1}	1.85/1.21	7.1×10^{11}	[123]
Ti ₃ C ₂ T _x /TiO ₂	PEC	0	360	0.1	2.1×10^{-3}	0.045/0.069	–	[124]
Ti ₃ C ₂ T _x /GaIn	FET	0	355	8.5	2.8×10^{-1}	7.55 μ s/1.67 ms	7.1×10^{13}	[125]
Ti ₃ C ₂ /Si	FET	0	910	0.7	4.0×10^{-1}	0.14 /0.16 ms	2.0×10^{13}	[126]
Ti ₃ C ₂ T _x /n-GaN	FET	0	365	4.3	4.4×10^{-2}	0.06/0.02	3.9×10^{12}	[127]
Ti ₃ C ₂ T _x /GaAs	FET	0	650	6.6	1.5	70.2/50.8 ms	1.2×10^{13}	[128]
Nb ₂ CT _x @Bi	PEC	0.8	350	1.6	5.9×10^{-4}	0.08/0.08	4.6×10^{12}	[100]
MoS ₂ /MXene	FET	1.0	750	4.9×10^2	1.9	< 0.15	2.1×10^{10}	[129]
Ti ₃ C ₂ T _x /Si	FET	1.0	638	5.8×10^3	3.0×10^1	9.53/14.26 μ s	7.7×10^{14}	[130]
CsPbBr ₃ QDs/Ti ₃ C ₂ T _x	FET	1.0	515	3.2×10^{-1}	1.1×10^{-4}	46.2/24.6 ms	$\sim 7 \times 10^8$	[131]
ReS ₂ /Ti ₃ C ₂ T _x	FET	2.0	VL ^b	1.0×10^4	4.1×10^1	3.7	1.1×10^{12}	[132]
ReS ₂ /Ti ₃ C ₂ T _x	FET	2.0	NL ^c	6.7×10^3	2.7×10^1	3.85	7.1×10^{11}	[132]
Ti ₃ C ₂ /ZnO	FET	5.0	240	–	1.3×10^{-1}	–	5.7×10^{11}	[133]
Ti ₃ C ₂ T _x -TiO ₂	FET	5.0	405	–	7.8×10^{-5}	0.694/0.812	8.4×10^4	[134]
Ti ₃ C ₂ /ε-Ga ₂ O ₃	FET	0	254	1.6×10^{-3}	1.6×10^{-2}	43/145 ms	2.2×10^{11}	[135]
Ti ₃ C ₂ Br/CsFAMA	FET	1	520	2.4×10^5	3.93	29.9 μ s	2.6×10^{12}	[136]
Ti ₃ C ₂ T _x /MoS ₂	FET	1	520	2.1×10^4	2.1×10^1	4.62/8.48	5.4×10^{12}	[137]

^a Light Wavelength.^b Visible Light.^c NIR light.^d Photocurrent Density.^e Photoresponsivity.^f Response time.^g Detectivity.

decay times, respectively) were observed. In addition, the Ti₃C₂T_x/TiO₂ showed excellent long-term stability, where the self-powered photocurrent showed no attenuation after 150 cycles and only 2% decrement was observed after the device was stored for one week. Similar characteristics were reported by Khatun et al., where the photoelectrochemical performance of Ti₃C₂T_x flakes functionalized TiO₂ nanotube arrays was studied (Fig. 10e) [144]. Tested by a traditional three-electrode PEC system, the photocurrent density reached maximum with a Ti₃C₂T_x content of 15%, which is about 200% higher than that of bare TiO₂ nanotubes. Further increasing the Ti₃C₂T_x content resulted in a decrement of the photocurrent and this could be ascribed to the agglomeration of MXene flakes, which results in a reduction of effective surface area and light absorption. According to the band diagram and working mechanism (Fig. 10f), the inter-band and intra-band transitions in Ti₃C₂T_x induce the LSPR effect, which further promotes the electron transfer from the MXene to the conduction band of TiO₂, resulting in an enhanced PEC performance. Very recently, Xiong et al. reported a large-area flexible photodetector based on a 3D-networked Ti₃C₂T_x-TiO₂ heterostructure [134]. The active materials were obtained *via* a controllable in-situ-oxidization strategy, where the in-situ oxidized derivative TiO₂ nanosheets were well-dispersed and connected within the multi-layer Ti₃C₂T_x, constituting a continuous 3D-networked structure. As illustrated in Fig. 10g, the photodetectors are constructed by drop-casting the Ti₃C₂T_x-TiO₂ composite followed by sputtering the metal electrodes on a paper substrate, which shows the advantages of excellent flexibility with low cost. Under the irradiation of

405 nm light (8.58 mW) with 5 V bias potential, the Ti₃C₂T_x-TiO₂ composite showed a responsivity of 0.078 mA/W and detectivity of 8.4×10^4 Jones, which are about 14 and 4200 times the values for pristine Ti₃C₂T_x MXene. The enhanced photoresponse performance can be ascribed to the increased excitation of photogenerated carriers as well as to the efficient conductive pathway for fast transfer of carriers in Ti₃C₂T_x-TiO₂ (Fig. 10h). Combining the excellent long-term stability (no attenuation after 5000 s irradiation), a large area optical imaging device (10×10 cm²) has been successfully fabricated based on photodetector arrays, which opens avenues for the application of MXene derivatives in photo- and environmental sensing.

Owing to the abundant terminations, MXene can be integrated with various active materials giving resultant composites that are promising materials for high-performance photodetectors. Combinations of MXenes with traditional photoresponsive materials, such as transition metal oxides, have been widely investigated and proved to further improve their performance [120,121,123,133]. For instance, Guo et al. demonstrated that the deep ultraviolet (DUV) photovoltaic performance of the Zn₂-GeO₄ crystal could be greatly enhanced by addition of 2D MXene flakes [120]. As shown in Fig. 10i, the Zn₂GeO₄ nanowires were directly grown on insulator substrates by a catalyst-free CVD method and the Ti₃C₂ flakes were subsequently drop-casted on the surface to form the active layer. Using two drops of silver paste as electrodes, the photoresponse performance was measured with a potentiostat under the irradiation of DUV light. Compared with the pure Zn₂GeO₄ nanowires, the addition of 0.03% MXene endowed enhancements of 150%, 153%, and

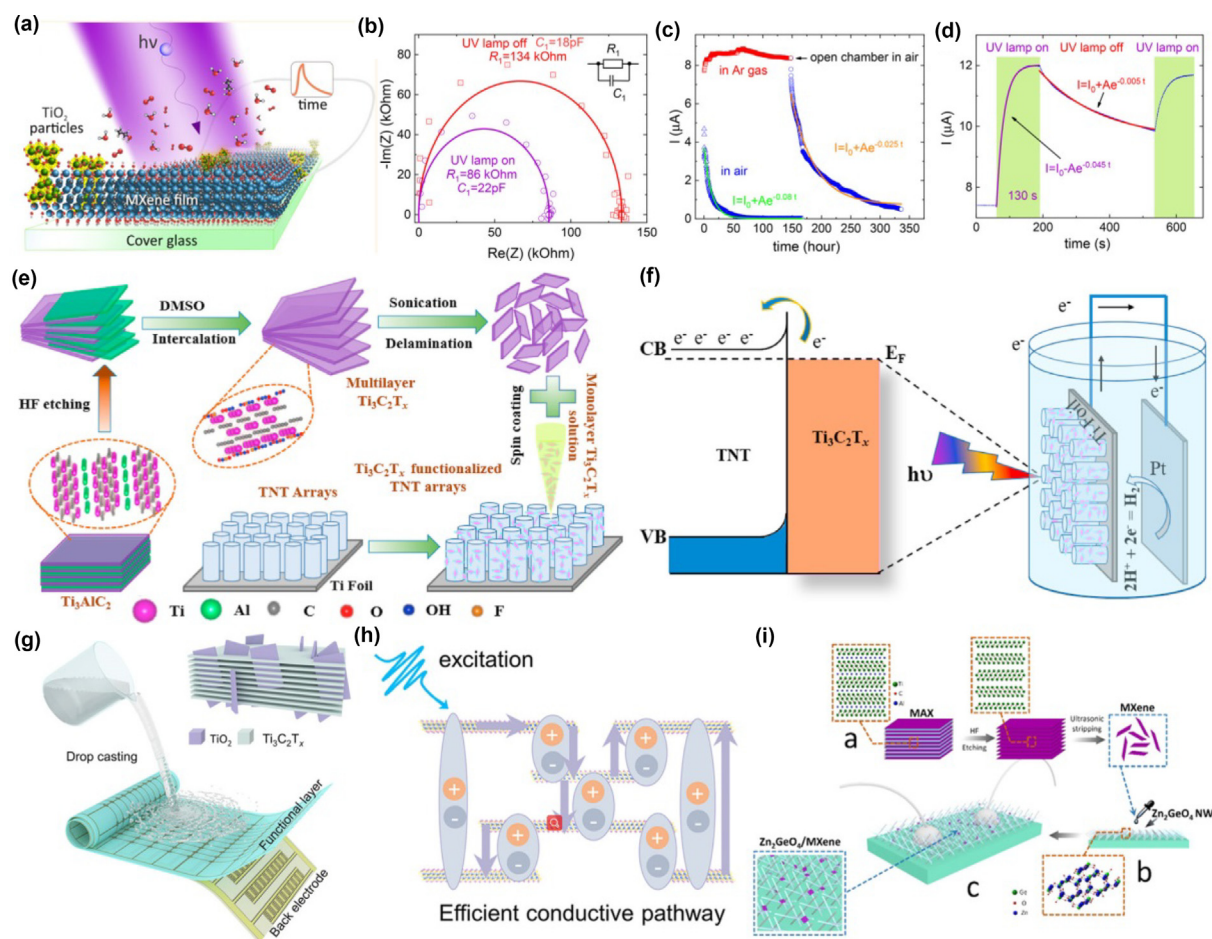


FIGURE 10

(a) Schematic illustration of a Ti_3C_2 - TiO_2 based photodetector. (b) Nyquist plots of a $\text{Ti}_3\text{C}_2\text{T}_x$ thin film with and without UV irradiation. (c) Chronoamperometry of $\text{Ti}_3\text{C}_2\text{T}_x$ thin film under various atmospheres. (d) Chronoamperometry of a $\text{Ti}_3\text{C}_2\text{T}_x$ thin film under argon with and without UV irradiation. Reproduced with permission [143]. Copyright 2018, American Chemical Society. (e) Functionalization of TiO_2 nanotube arrays with $\text{Ti}_3\text{C}_2\text{T}_x$ flakes. (f) Band diagram and working mechanism of PEC water splitting of functionalized TiO_2 nanotube arrays. Reproduced with permission [144]. Copyright 2022, Elsevier. (g) Large-area fabrication process of a scalable photodetector based on a 3D-networked $\text{Ti}_3\text{C}_2\text{T}_x$ - TiO_2 composite. (h) Efficient carrier transport processes over a 3D-networked $\text{Ti}_3\text{C}_2\text{T}_x$ - TiO_2 heterostructure. Reproduced with permission [134]. Copyright 2022, Elsevier. (i) Synthesis of crossed Zn_2GeO_4 NWs/MXenes. Reproduced with permission [120]. Copyright 2020, American Chemical Society.

60% for responsivity, EQE, and response time, respectively. The enhanced photoresponse performance are mainly due to the synergistic effect of Ti_3C_2 and Zn_2GeO_4 nanowires, where the conductive MXene promotes the carrier transport and the large contact interfaces accelerate the separation of electron-hole pairs. Li et al. established an efficient carrier transportation channel by blending 0D ZnO QDs and 2D $\text{Ti}_3\text{C}_2\text{T}_x$ nanoflakes, which confines the light within the photoactive layers and enhances the sensitivity of photodetection [123]. Owing to the localized surface plasmon resonance effect of the MXene, the light absorption of ZnO/ $\text{Ti}_3\text{C}_2\text{T}_x$ film is enhanced and an impressively improved EQE (150%) was achieved. In addition, an optimal responsivity of 425 mA/W with fast response time was observed due to the fast carrier transportation and accelerated hot electron injection between MXene and ZnO. Very recently, Song et al. also investigated the DUV photoresponse of the ZnO/ $\text{Ti}_3\text{C}_2\text{T}_x$ composite, where the 2D Ti_3C_2 nanoflakes were anchored on the surface of the ZnO film [133]. The introduction of the MXene enhanced the deep-UV band absorption while the formed van der Waals heterojunctions can create surface depletion and passivation,

which further suppresses the dark current and enhances the photocurrent. Compared with the pristine ZnO film, the on/off ratio, EQE, responsivity, and detectivity of the ZnO/ $\text{Ti}_3\text{C}_2\text{T}_x$ composite was enhanced by 284, 72, 74, and 55 times under the irradiation of 240 nm, respectively, which extends the application of the MXene to solar blind photodetectors.

Recently, perovskites materials have received enormous attention due to the excellent optical and electrical properties, and their integrations with MXenes have been extensively investigated [122,131,136,145]. In 2019, Pan et al. developed an in-situ growth strategy for all-inorganic CsPbX_3 perovskite nanocrystals on $\text{Ti}_3\text{C}_2\text{T}_x$ MXene (Fig. 11a) [145]. As revealed, the perovskite nanocrystals are well-dispersed on the MXene surface, constructing efficient transportation highways for the photo-generated carriers. The MXene/ CsPbX_3 composites show significant photoluminescence quenching and shorter photoluminescence decay lifetimes, indicating an improved excited state charge transfer process. As can be seen in Fig. 11b, the resultant devices can response to both visible and X-ray light owing to the increased photocurrent generation. Very recently, Li et al. also

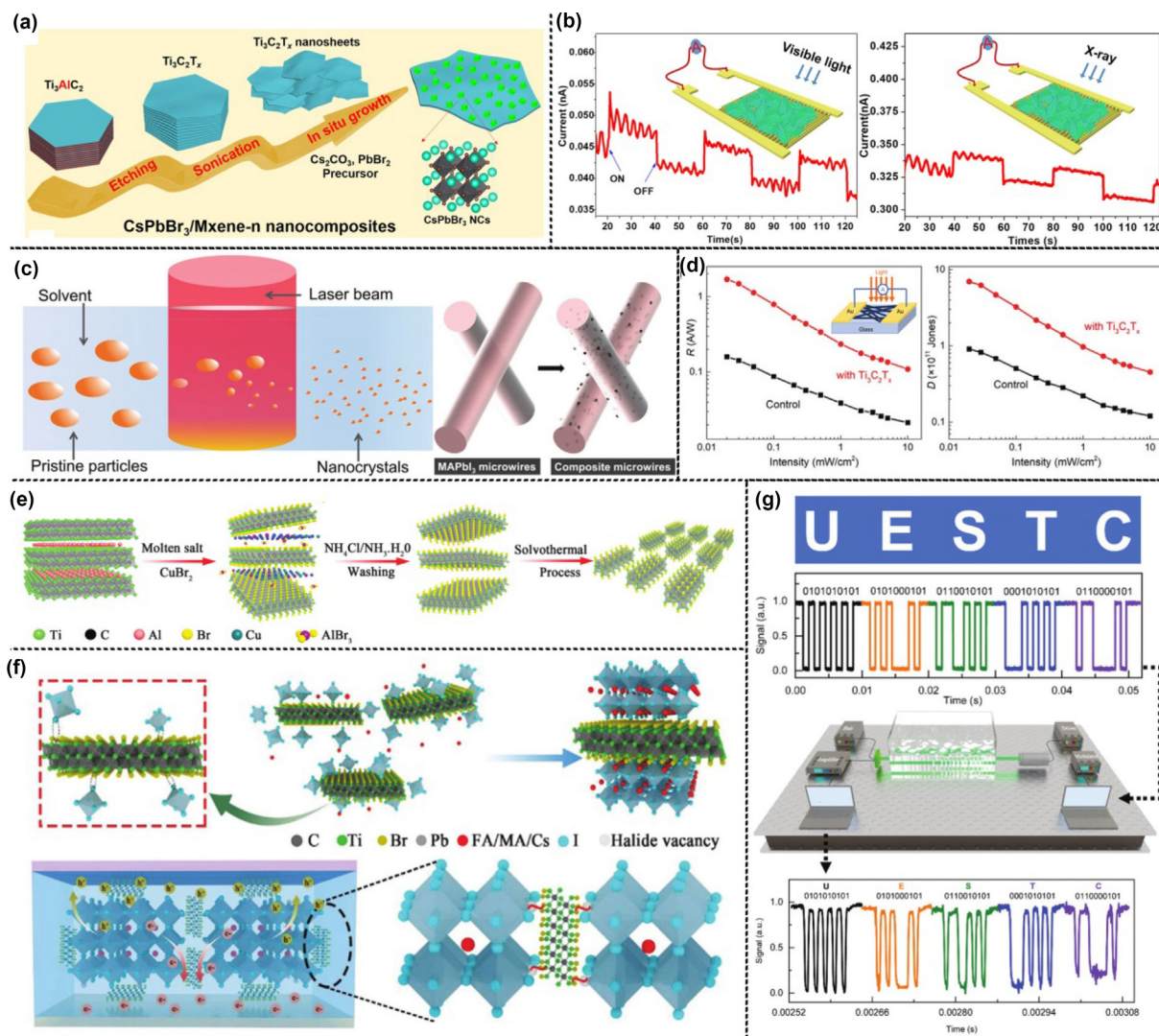


FIGURE 11

(a) Schematic illustration of the in-situ growth of CsPbBr₃ NCs on MXene flakes. (b) Photo-response performances of CsPbBr₃ NCs/MXene under the irradiation of white LED and X-ray. Reproduced with permission [145]. Copyright 2019, American Chemical Society. (c) Synthesis of Ti₃C₂T_x NCs and the corresponding embedded MAPbI₃ microwires. (d) The responsivity and detectivity of embedded MAPbI₃ microwires as function of light intensity. Reproduced with permission [122]. Copyright 2021, Wiley-VCH. (e) Synthesis of Br-terminated Ti₃C₂T_x by molten-salt etching and hydrothermal approach. (f) Schematic mechanism of introducing Br-terminated Ti₃C₂T_x in the perovskite film. (g) An underwater wireless optical communication system based on a perovskite photodetector modified with Br-terminated Ti₃C₂T_x. Reproduced with permission [136]. Copyright 2022, Royal Society of Chemistry.

investigated the photoresponse of Ti₃C₂T_x/CsPbX₃, where the hybrid was obtained by a facile assembling approach [131]. According to the SEM images, the MXene flakes were uniformly distributed after a simple blending. Owing to the spontaneously intensified surface electromagnetic fields of Ti₃C₂T_x, incident fugacious photons in the CsPbBr₃ film can be successfully confined, which accelerates the transportation of photo-generated carriers in the composite. Compared with the pristine CsPbBr₃, the photo-response performance of the Ti₃C₂T_x/CsPbBr₃ device increases as a function of the MXene content due to the excited hot electrons while the EQE was intensified by 300% under the irradiation of 490 nm light (2.9 mW/cm²).

In addition to the inorganic perovskites, organic-inorganic hybrids have also been integrated with MXenes to further enhance charge separation and transfer. In order to improve the internal carrier transport of MAPbI₃ microwires and the

mobility of integrated films simultaneously, Ti₃C₂T_x nanocrystals were deposited on the MAPbI₃ microwires [122]. As shown in Fig. 11c, the colloidal Ti₃C₂T_x nanocrystals were synthesized via a non-focus laser irradiation strategy with a pulsed laser and subsequently hybridized into MAPbI₃ microwires. The introduction of a conductive Ti₃C₂T_x colloidal could enhance the crystalline orientation of the perovskite crystals since the defects in the MAPbI₃ microwires are reduced by the -F terminations on Ti₃C₂T_x. Exploiting the advantages of enhanced charge transport and carrier extraction as well as the promoted mobility, the as-prepared photodetector exhibited excellent performance with responsivity of 1.7 A/W and detectivity of 7.0×10^{11} Jones (Fig. 11d). A similar defect passivation phenomenon was also observed in metal halide perovskite modified with bromide-terminated Ti₃C₂ MXene nanoparticles (Br-MNP) [136]. As can be seen in Fig. 11e, the Br-MNPs were fabricated through the

combination of a molten-salt etching method and a hydrothermal process. By blending Br-MNPs in the perovskite, the halide vacancies were effectively compensated by the Br terminations and the crystallization process was spontaneously improved, promoting the formation of a better film morphology with enlarged vertical-oriented single grains and reduced trap state density (Fig. 11f). Taking the Br-MNPs as bridges between adjacent perovskite grains, the carrier transport was enhanced with mobility as high as $0.21 \text{ cm}^2 \cdot \text{V}^{-1} \cdot \text{s}^{-1}$, resulting in an optimized responsivity of 3.93 A/W and response time of $29.9 \mu\text{s}$. Moreover, an underwater wireless optical communication system has been achieved based on the modified perovskites, where the encoded signals can be clearly identified (Fig. 11g). We conclude that the integration of MXenes paves the way for a new strategy for defect management of perovskites, while the improvement of the photo-response performance and the working mechanism need more efforts.

Several successful combinations of MXenes with conventional III–V semiconductors have been reported, where the 2D MXenes can be stacked onto target substrates by physical transfer/deposition [125,127,128]. In 2021, Song et al. created a $\text{Ti}_3\text{C}_2\text{T}_x/\text{GaN}$ van der Waals heterojunction (vdWH) and proposed a

highly efficient ultraviolet photodiode with stable current outputs [125]. As shown in Fig. 12a, the MXene colloid was sprayed onto the GaN substrate to obtain the arrays while the contact area was controlled by various masks. InGa were produced on GaN as electrodes and their ohmic contact was confirmed by linear I – V properties of the device without MXene (Fig. 12b). In the MXene/GaN vdWH photodiode, typical rectification features are observed when the I – V curves are presented on a linear scale, indicating the formation of a Schottky barrier between MXene and GaN. As shown in Fig. 12c, a built-in electric field can spontaneously form at Schottky junction and promote the separation of photocarriers. Benefiting from the photoexcited hot carriers produced by the $\text{Ti}_3\text{C}_2\text{T}_x$ MXene under UV light, an ultrahigh internal quantum efficiency (IQE) over 100% and EQE over 99% could be achieved at self-powered mode. Under the irradiation of a low power density ($30 \mu\text{W}/\text{cm}^2$), the self-powered responsivity and detectivity could reach 284 mA/W and $7.06 \times 10^{13} \text{ Jones}$, respectively. Yi et al. also investigated the self-driven photo-response of $\text{Ti}_3\text{C}_2\text{T}_x/(\text{n/p})\text{-GaN}$ heterostructures, where the Schottky contacts of $\text{Ti}_3\text{C}_2\text{T}_x$ with both n-GaN and p-GaN were confirmed by ultraviolet photoelectron spectroscopy [127]. The photodetector based on $\text{Ti}_3\text{C}_2\text{T}_x/\text{n-GaN}$ exhi-

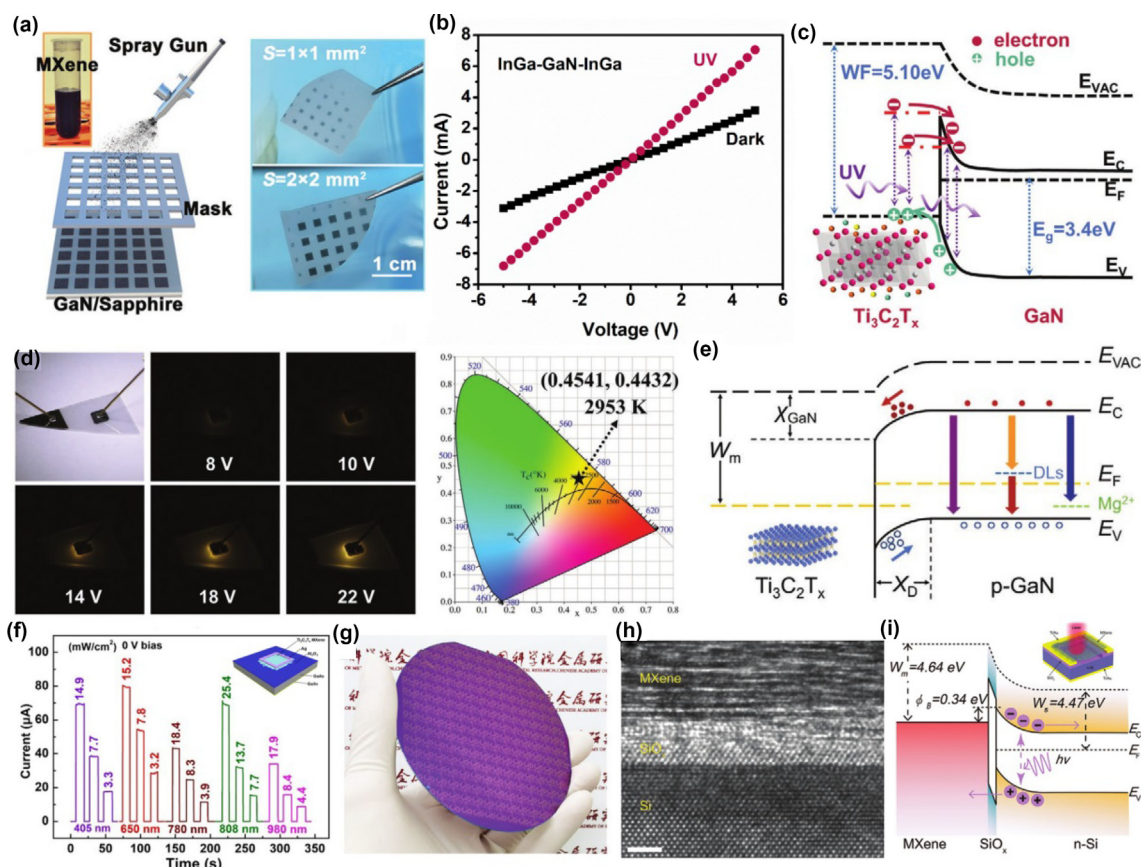


FIGURE 12

(a) The deposition of Ti_3C_2 MXene onto GaN via spray-deposition method using a mask to define the contacting area. (b) I – V characteristic of the InGa/GaN/InGa device under dark and UV illumination. (c) Energy band diagram of $\text{Ti}_3\text{C}_2/\text{GaN}$ heterojunction based on calculation. Reproduced with permission [125]. Copyright 2021, Wiley-VCH. (d) The optical pictures and CIE chromaticity diagram of the $\text{Ti}_3\text{C}_2\text{T}_x/\text{p-GaN}$ heterostructure LEDs. (e) The band diagram of the $\text{Ti}_3\text{C}_2\text{T}_x/\text{p-GaN}$ heterostructure LED under forward bias. Reproduced with permission [127]. Copyright 2021, Wiley-VCH. (f) The time-dependent photo-response of the $\text{Ti}_3\text{C}_2\text{T}_x/\text{GaAs}$ device under different wavelengths and light power densities. Reproduced with permission [128]. Copyright 2021, Elsevier. (g) Patterned $\text{Ti}_3\text{C}_2\text{T}_x$ film on a 4-inch Si wafer. (h) TEM image of the $\text{Ti}_3\text{C}_2\text{T}_x/\text{Si}$ interface. (i) Band diagram of the $\text{Ti}_3\text{C}_2\text{T}_x/\text{Si}$ photodetector under illumination – the inset shows the schematic illustration of the device. Reproduced with permission [130]. Copyright 2022, Wiley-VCH.

bits fast response times (rise time of 60 ms and decay time of 20 ms), a high responsivity of 44.3 mA/W, and an excellent on/off ratio of $\sim 1.13 \times 10^4$ under the irradiation of 365 nm light ($96.9 \mu\text{W}/\text{cm}^2$). In addition, the integration of MXene/III–V semiconductors can also endow device novel properties. For instance, the light emitting diodes based on $\text{Ti}_3\text{C}_2\text{T}_x/\text{p-GaN}$ show stable orange light emission under various bias potentials (Fig. 12d). According to the proposed mechanism in Fig. 12e, the holes in $\text{Ti}_3\text{C}_2\text{T}_x$ can transfer to p-GaN under a bias potential and recombine with electrons, leading to the emission of various light wavelengths, such as ultraviolet light at 376 nm from the near-band emission, blue light (436 nm) from the Mg-acceptor-related emission and orange/red light (602/706 nm) from deep-level emissions of p-GaN. In addition, a broadband self-driven photodetector has been developed based on a $\text{Ti}_3\text{C}_2\text{T}_x/\text{GaAs}$ Schottky heterojunction [128]. As shown in Fig. 12f, the photocurrent increases with the increment of light power density under the irradiation of light with various wavelengths, which can be ascribed to the broad-band absorption of the $\text{Ti}_3\text{C}_2\text{T}_x$ layer and the high-quality $\text{Ti}_3\text{C}_2\text{T}_x/\text{GaAs}$ interaction. Due to the fast generation of hot electrons in the MXene layer, the sensing range of this $\text{Ti}_3\text{C}_2\text{T}_x/\text{GaAs}$ photodetector was extended to the infrared region, which shows apparent response to 980 nm light.

Moreover, the photo-response performance of traditional silicon semiconductors has been enhanced by the design of heterostructures with MXenes and interface engineering of interfacial SiO_x layers [126,130]. As revealed, the dark current can be reduced by the improved interface quality, which is achieved by growing the interfacial SiO_x layers and controlling the thickness of the $\text{Ti}_3\text{C}_2\text{T}_x$. The oxidation of MXene flakes were prevented after encapsulation with silicone, endowing a photodetector excellent stability with high EQE ($\sim 54\%$) and specific detectivity ($\sim 2.09 \times 10^{13}$ Jones) [126]. Taking advantage of the outstanding film-forming ability, a wafer-scale MXene film could be patterned on a large-area SiO_2/Si substrate *via* photolithography and dry etching techniques, where patterns with sharp edges and micro-scale resolution (up to 2 μm) were achieved (Fig. 12g) [130]. As shown in Fig. 12h, a plane-to-plane stacking of $\text{Ti}_3\text{C}_2\text{T}_x$ can be observed while there is one layer of SiO_x between $\text{Ti}_3\text{C}_2\text{T}_x$ MXene and n-Si. As mentioned above, the interfacial SiO_x layer can reduce the dark current, resulting in an excellent detectivity as high as 7.73×10^{14} Jones. Accord-

ing to the proposed working mechanism (Fig. 12i), there is a built-in electric field under reverse bias potential, which promotes the separation of photo-generated carriers and subsequently enhances the photocurrent. The $\text{Ti}_3\text{C}_2\text{T}_x/\text{n-Si}$ photodetector also exhibits high stability and reliability, where the photocurrent is unchanged after 15,000 cycles. In addition, a fully-monolithic image sensor array with 1024 pixels was achieved based on the $\text{Ti}_3\text{C}_2\text{T}_x/\text{n-Si}$ heterojunction and a high contrast with sharp edges could be observed, extending the application of the MXene-based composites to the field of micro-nanoelectronics.

For the fabrication of MXene-based heterojunctions, one can use a physical strategy (such as mechanical blending or physical transfer/deposition) based on the as-fabricated precursor materials [129,132,135,137]. For instance, Zhu et al. synthesized triangular monolayer MoS_2 on an SiO_2/Si substrate by a hydroxide-assisted method and a $\text{MoS}_2/\text{Ti}_3\text{C}_2\text{T}_x$ heterostructure was obtained by a following spin-coating $\text{Ti}_3\text{C}_2\text{T}_x$ suspension [129]. It should be noted that the heterostructures were randomly formed on the substrate, making it a bit complicated to practically fabricate the device. Using a similar procedure, a hybrid plasmonic structure was achieved based on MXene nanoparticles (MNPs) and MoS_2 nanosheets, where the MoS_2 nanosheets were firstly fabricated by a CVD approach on Si/SiO_2 substrates and the MNPs were directly spin-coated [137]. Owing to the intense electromagnetic fields generated by strong localized surface plasmon resonances of the MXene flakes, the photodetector exhibited enhanced responsivity (20.67 A/W), detectivity (5.39×10^{12} Jones), and an extremely high EQE value of 5167%. On the other hand, MXene-based composites can also be obtained by the bottom-up strategy, such as in-situ growth of Bi QDs on an Nb_2C substrate by a hydrothermal reaction [100]. The obtained $\text{Nb}_2\text{CT}_x/\text{Bi}$ Schottky heterojunctions exhibited excellent self-powered capability with high responsivity. In contrast, in-situ growth of MXenes on other materials is still under investigation and calls for more efforts. The morphology and structure of the composites are more specific based on the bottom-up strategy, which is beneficial for investigations of the mechanisms. However, the physical strategy has been more commonly used in recent years for the fabrication of MXene-based heterojunctions owing to the facile procedures and the possibilities for quantitative preparation.

TABLE 3

Compared photo-response performance of pristine MXenes as active materials.

Materials	Structure	Voltage (V)	λ^a (nm)	P_{ph}^c ($\mu\text{A}/\text{cm}^2$)	R_{ph}^d (A/W)	$t_{\text{res}}/t_{\text{rec}}^e$ (s)	D^{*f} (Jones)	Ref.
Mo_2CT_x	FET	1.0	660	4.5×10^3	9.0	–	5×10^{11}	[96]
ScC_xOH	FET	10.0	360	2.0×10^1	1.3×10^{-1}	–	–	[27]
$\text{Ti}_3\text{C}_2\text{T}_x$	Capacitive	1.0	SL ^b	3.5	3×10^{-5}	–	–	[146]
Nb_2C	PEC	0.8	400	0.2	2.8×10^{-5}	0.15/0.1	–	[147]
Nb_2C	FET	1.0	405	2.4×10^2	4.6×10^{-1}	2.95/3.82	–	[147]
Nb_2C	Photothermal	–	405	–	$8.2 \times 10^1 \text{ nm}/\text{W}\cdot\text{cm}^{-2}$	0.1/0.07	–	[148]

^a Light Wavelength.^b Solar Light.^c Photocurrent Density.^d Photoresponsivity.^e Response time.^f Detectivity.

Pristine MXenes

Taking the advantages of low-cost fabrication and tunable electronic structures into account, pristine MXenes have also been directly applied as active materials for various photodetectors. The corresponding parameters and performance data are summarized in Table 3. In 2016, Lipatov et al. construct a field-effect transistor based on $\text{Ti}_3\text{C}_2\text{T}_x$ MXene to investigate the environmental stability by measuring the correspondent resistivity (Fig. 13a) [22]. As revealed, the resistivity of individual

flakes is only one order of magnitude lower than the multilayer $\text{Ti}_3\text{C}_2\text{T}_x$, indicating a good electron transport through the surface terminations of different flakes. Under humid air atmosphere, the drain-source current decreased with time after the initial exponential decay, which can be ascribed to the edge oxidation as confirmed by the AFM images (Fig. 13b). Taking advantage of the strong localized surface plasmon resonances and flexibility, MXene flakes can be utilized as active materials for plasmonic photodetectors [96]. As shown in Fig. 13c, MXene

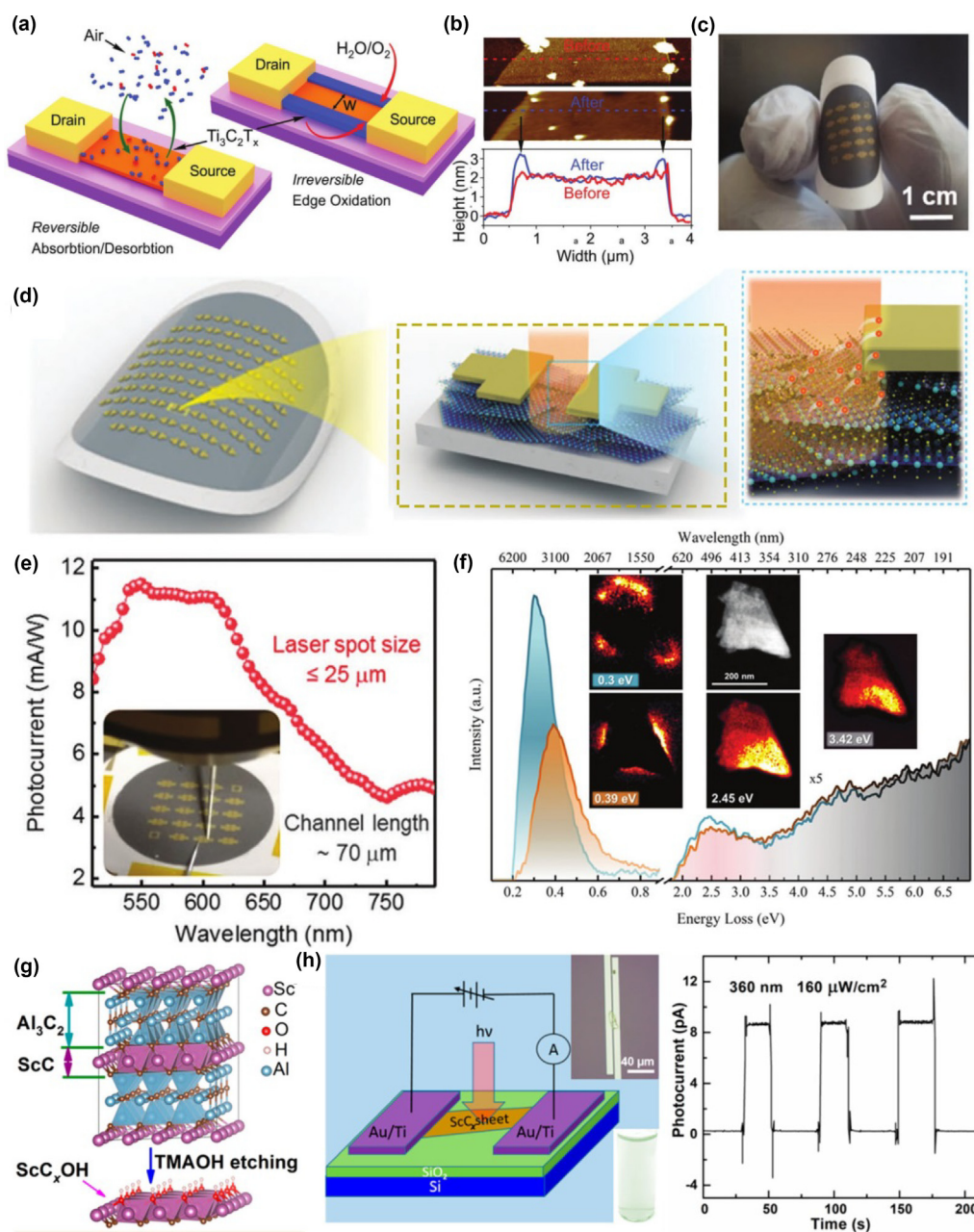


FIGURE 13

(a) Schematic illustration of reversible molecular adsorption and edge oxidation for a $\text{Ti}_3\text{C}_2\text{T}_x$ -based FET photodetector. (b) AFM images of $\text{Ti}_3\text{C}_2\text{T}_x$ -based FET before and after exposure to air. Reproduced with permission [22]. Copyright 2016, Wiley-VCH. (c) Photograph Mo_2CT_x -based flexible photodetector. (d) Working mechanism of Mo_2CT_x -based flexible photodetector. (e) Photo-response of Mo_2CT_x -based photodetector as a function of wavelength. (f) Scanning transmission electron microscopy and ultrahigh resolution electron energy loss spectroscopy of Mo_2CT_x . Reproduced with permission [96]. Copyright 2019, Wiley-VCH. (g) Selective etching of Al_3C_2 from ScAl_3C_3 compound. (h) Schematic illustration of the photodetector based on ScC_xOH and its photo-response under the irradiation of 360 nm light. Reproduced with permission [27]. Copyright 2019, American Chemical Society.

flakes have been deposited on a nylon paper membrane by filtration and Au electrodes were fabricated on the MXene film by beam evaporation to construct the photodetector. Fig. 13d shows the migration process of the plasmon-assisted hot carriers toward the biased gold electrodes. Two needle-shaped probes were pinned on Au electrodes to measure the photocurrent of the MXene-based device under the irradiation of visible light ranging from 400 to 800 nm (Fig. 13e). In addition to the traditional $\text{Ti}_3\text{C}_2\text{T}_x$, the photo-response performance of other kinds of MXenes (such as Mo_2CT_x , Nb_2CT_x , T_2CT_x , and V_2CT_x) has also been revealed. Among these MXenes, Mo_2CT_x exhibits

the best results with responsivity up to 9 A/W and detectivity as high as $\sim 5 \times 10^{11}$ Jones. The spatial and energy distribution of surface plasmon modes over the Mo_2CT_x nanosheets can be imaged by means of scanning transmission electron microscopy and ultrahigh resolution electron energy loss spectroscopy (Fig. 13f). Moreover, the dynamics of the generated plasmon-assisted hot carriers in Mo_2CT_x flakes were investigated by femtosecond visible transient absorption measurements, where the short lifetime coupling with light and dephasing of surface plasmons endow the Mo_2CT_x -based device an excellent photo-response ability.

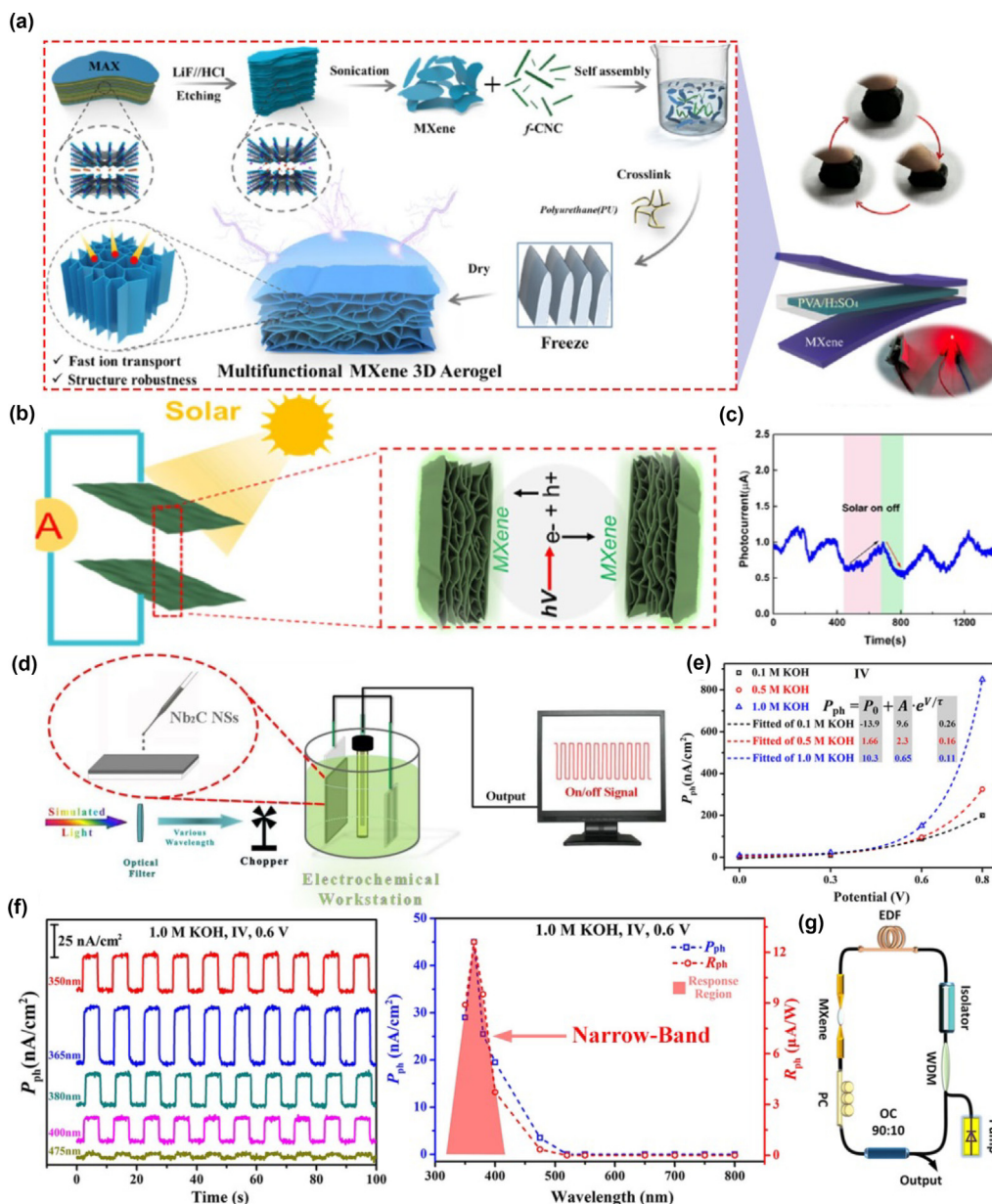


FIGURE 14

(a) Constructing MXene 3D-Aerogel by bio-inspired freezing approach and assembly of MXene-based supercapacitor. (b) Working mechanism of the photoresponsive supercapacitor. (c) Photo-response performance of MXene-based supercapacitor. Reproduced with permission [146]. Copyright 2021, American Chemical Society. (d) PEC system built for evaluating the photo-response behavior of Nb_2C -based photodetector. (e) The calculated photocurrent density as a function of the bias potential in various KOH concentrations. (f) On/off switching behavior of Nb_2C -based photodetector under the irradiation of various wavelengths and the photo-response performance as a function of wavelength. (g) Experimental setup of an Er-doped PML fiber laser based on Nb_2C MXene. Reproduced with permission [147]. Copyright 2021, American Chemical Society.

Generally, semiconducting properties are necessary for optoelectronics while the photo-generated carriers undergo fast recombination in a conductive material, indicating that the metallic nature of MXenes is disadvantageous for photodetection. In 2019, Zhou et al. demonstrated the first direct band gap MXene, namely ScC_xOH , which was obtained by selective organic-base etching of a non-MAX ScAl_3C_3 precursor (Fig. 13g) [27]. Combining the experimental studies and first-principles density functional theory calculations, the ScC_xOH MXene was predicted with a direct band gap of ~ 2.5 eV, facilitating its further application for ultraviolet-visible light detection. As shown in Fig. 13h, apparent on/off signals can be observed from the ScC_xOH -based FET device under the irradiation of light with 360 nm and $160 \mu\text{W}/\text{cm}^2$, where the overshooting indicates the existence of a few traps. In addition, theoretical calculations indicate that a conducting-like behavior can be achieved by surface modifications of various MXenes [24]. For instance, Mo_2CT_x and $\text{Mo}_2\text{TiC}_2\text{T}_x$ are predicted to possess indirect band gaps. The relevant photo-response performance and working mechanisms though need further investigations [149,150].

In addition to the traditional FET-type photodetectors, several different photodetection devices have been constructed owing to the unique properties of MXenes [146–148]. For instance, a high-performance photo-responsive supercapacitor has been revealed by Cai et al., where multifunctional MXene aerogels are assembled via a bio-inspired freezing approach and utilized as working electrodes (Fig. 14a) [146]. As illustrated in Fig. 14b, the separated electrons might move between two MXene electrodes when the supercapacitor is fully charged and the carriers could recombine quickly under light irradiation, resulting in an enhancement of leakage current. Through the detection of the leakage current, obvious on/off signals could be observed (Fig. 14c) and the photocurrent was found to increase with the increment of solar power intensity.

Recently, a novel PEC-type photodetector has been demonstrated based on a few-layer Nb_2C MXene, where the device could work under a liquid-phase condition (Fig. 14d) [147]. As can be seen in Fig. 14e, the photocurrent density increases with the increment of bias potential and electrolyte concentration, where the effect of bias potential is more significant. Although the photocurrent density and photoresponsivity are low relative to traditional FET-type photodetectors, the Nb_2C -based PEC-type device exhibits a narrow-band detection feature (Fig. 14f) and paves the way for a potential underwater communication application of pristine MXenes. In addition, an optical switch for passively mode-locked fiber lasers has been demonstrated by depositing Nb_2C nanosheets on tapered fibers, and ultrastable pulses could so be achieved in the telecommunication and mid-infrared regions (Fig. 14g). It has been revealed that Nb_2CT_x MXene has a high thermal conductivity and excellent photothermal conversion efficiency from visible to near-infrared wavelengths. Taking this advantage into account, a fiber-based all-optical photodetector has been demonstrated by coating MXene flakes on the surface of a microfiber, which was shown to exhibit broadband response with high sensitivity and fast response [148]. In addition to the photodetector, the deposition of 2D MXenes on specific fibers can also be used to construct various devices, such as all-optical switching and salinity sensors,

and here more efforts to further broaden the application prospects of pristine MXenes can be envisaged [83,151,152].

Conclusion and outlook

Owing to their controllable physicochemical properties, MXenes have been proven as promising building blocks for constructing photodetection devices. The recent five years have witnessed a rapid development of MXene-based photodetectors that exhibit unique performance such as being self-powered, narrowband, solar blind and broadband responsive. In this review, we briefly introduced the synthetic strategies for pristine MXenes and reviewed their properties mainly focusing on the optical and electronic aspects, which are essential for their performance in photodetectors. We comprehensively summarized the characteristics of MXene-based photodetectors with various constructions for practical applications, where the MXenes can serve as not only electrodes but also active materials. Owing to the tunable optoelectronic features, MXenes are by now widely used as electrodes for FET-type photodetectors, but prevail still at an early stage. For instance, taking the advantage of strong van der Waals forces between MXenes and traditional semiconductors Schottky contacts can subsequently be formed. The photo-response of MXene-based composites is the subject for ongoing research leading to successive improvements, and will probably soon become a mainstream in photodetector technology. Various photodetector constructions have been demonstrated based on pristine MXenes, indicating the direct use MXenes as active materials in such devices. With the fast growth of the MXene family of chemical compositions and the further revelation of interesting properties, the research on MXene-based photodetectors will be even more attractive.

Although pristine MXenes and corresponding composites have been extensively investigated in the photodetection field, their applications are still marginally explored and there remain several challenges to be addressed before routine practical applications can take place. Fig. 15 summarizes future research directions for

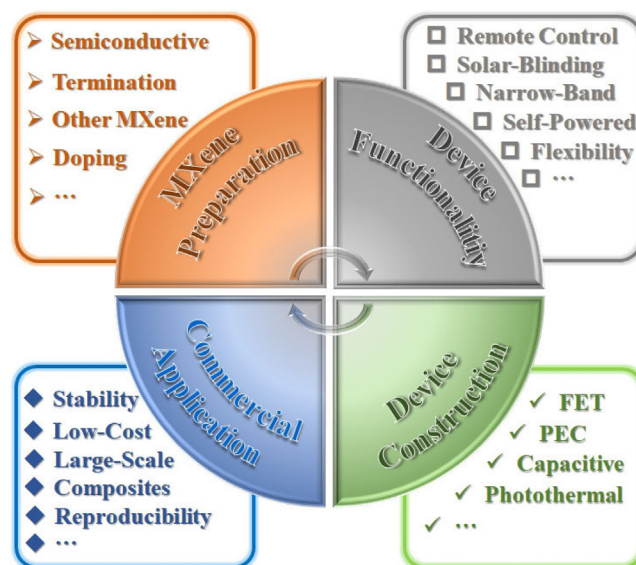


FIGURE 15

Summarized future research directions for MXene-based photodetectors.

MXene-based photodetectors, which can be divided into four main parts, including MXene preparation, device functionality, device construction, and commercial application. For the preparation of MXenes, over 80% examples have focused on the metallic Ti_3C_2 MXene, while less investigations have been devoted to other MXenes. Although over 40 kinds of MXenes have been experimentally synthesized and hundreds more are theoretically predicted, more efforts are required to explore the photo-response of a wider group of MXenes, especially those with semiconducting properties, to reveal the full potential. The optoelectric properties of pristine MXene can be tuned by composition and surface terminations, resulting in suitable band-structure and work function for photodetection. In addition, the elemental doping strategy has proved to be effective for optimizing their properties, which will be beneficial for the achievements of various functionalities. Based on the different roles of MXenes and their structural design, some particular functionalities have been achieved, such as narrow-band detection, self-powered response and solar-blinding. However, more efforts are required to extend their application scenarios by endowing MXene-based photodetectors with more novel functionalities, such as under-water and remote control detection in harsh environments.

As regard to the device structures, several unique constructions have been revealed, such as capacitive-, photothermal-, and photoelectrochemical-type photodetectors, which can further extend the practical applications of MXene-based photodetectors. However, the working mechanisms for those constructions have so far mostly been based on calculated electronic structure and energy band diagrams, and a large numbers of experimental techniques are called for to verify the simulated structures and characteristics of the MXenes, such as spatially resolved electron energy-loss spectroscopy, scanning Kelvin probe force microscopy and ultrafast femtosecond transient absorption spectroscopy. In addition, MXenes have been widely applied in the field of energy storage such as in supercapacitors and in rechargeable batteries, which can be directly applied as power supply systems for MXene-based photodetectors, making it possible achieve all-MXene photodetectors. Facing commercial applications, the stability and fabrication costs are main concerns. The oxidation of MXenes is an inevitable issue, which penetrates the whole history of the device from construction to use. Although the combination with conventional active materials have improved the performance of the resultant photodetectors, the direct utilization of pristine MXene can further decrease the fabrication cost and facilitate large-scale implementations. Considering the excellent processability, MXene inks can be used on complicated substrates for volume production *via* various printing and coating technologies, facilitating the achievement of flexible MXene-based photodetectors with large area.

This review summarized the recent advances of MXene-based photodetectors and their current merits, limitations and challenges were presented in detail, which we believe can enlighten their future development. Although the research on MXene-based photodetectors still can be considered to be at its infancy, we anticipate that the diverse functionalities and unique optoelectric properties of MXenes will keep them in a forefront position for photodetection over a long period of time.

Data availability

Data will be made available on request.

Declaration of Competing Interest

The authors declare that they have no known competing financial interests or personal relationships that could have appeared to influence the work reported in this paper.

Acknowledgements

Gao L. and Zhao Y. contributed equally to this work. The research was supported by the National Natural Science Foundation of China (Grant Nos. 62005177, 61875138 and 61961136001), start-up funding from Hangzhou Normal University (Pandeng II Plan Foundation: 2021QDL036), Key Project of Department of Education of Guangdong Province (no. 2018KCXTD026), Program of Henan Center for Outstanding Overseas Scientists (GZS2020011). Authors acknowledge support and funding of King Khalid University through Research Center for Advanced Materials Science (Grant no: RCAMS/KKU/006/21).

References

- [1] D. Marpaung et al., *Nat. Photonics* 13 (2) (2019) 80–90.
- [2] F. Rothmayr et al., *Appl. Phys. Lett.* 112 (16) (2018) 161107.
- [3] F. Yan et al., *Small Methods* 2 (5) (2018) 1700349.
- [4] T. Liu et al., *Chinese Phys. B* 28 (1) (2019) 017302.
- [5] G. Konstantatos, *Nat. Commun.* 9 (1) (2018) 1–3.
- [6] C. Xie et al., *Adv. Funct. Mater.* 27 (19) (2017) 1603886.
- [7] F. Koppens et al., *Nat. Nanotechnol.* 9 (10) (2014) 780–793.
- [8] M. Naguib et al., *Adv. Mater.* 23 (37) (2011) 4248–4253.
- [9] J. Zou et al., *Chem. Soc. Rev.* 51 (8) (2022) 2972–2990.
- [10] L. Gao et al., *Chem. Mater.* 32 (5) (2020) 1703–1747.
- [11] L. Gao et al., *Adv. Mater.* 33 (10) (2021) 2004129.
- [12] Y.-Z. Zhang et al., *Chem. Soc. Rev.* 49 (20) (2020) 7229–7251.
- [13] L.X. Liu et al., *Adv. Funct. Mater.* 29 (44) (2019) 1905197.
- [14] Y. Yuan et al., *Adv. Mater.* 34 (12) (2022) 2110013.
- [15] Y. Zhang et al., *Nature* 438 (7065) (2005) 201–204.
- [16] Y. Shi et al., *Chem. Soc. Rev.* 44 (9) (2015) 2744–2756.
- [17] J. Cheng et al., *Nano-Micro Lett.* 12 (1) (2020) 1–13.
- [18] Q. Zhou et al., *Angew. Chem. Int. Ed.* 55 (38) (2016) 11437–11441.
- [19] H. Xu et al., *Adv. Funct. Mater.* 30 (24) (2020) 2000907.
- [20] B. Wang et al., *Chem. Eng. J.* 403 (2021) 126336.
- [21] J.S. Meena et al., *Electron. Mater.* 18 (3) (2022) 256–274.
- [22] A. Lipatov et al., *Adv. Electron. Mater.* 2 (12) (2016) 1600255.
- [23] T.L. Tan et al., *ACS Nano* 11 (5) (2017) 4407–4418.
- [24] J. Halim et al., *Adv. Funct. Mater.* 26 (18) (2016) 3118–3127.
- [25] J. Zhou, et al., *Angew. Chem., Int. Ed.* 55 (16) (2016) 5008–5013.
- [26] J. Zhou et al., *ACS Nano* 11 (4) (2017) 3841–3850.
- [27] J. Zhou et al., *ACS Nano* 13 (2) (2019) 1195–1203.
- [28] J. Halim et al., *Chem. Mater.* 26 (7) (2014) 2374–2381.
- [29] V. Natu et al., *Chem* 6 (3) (2020) 616–630.
- [30] M. Ghidui et al., *Nature* 516 (7529) (2014) 78–81.
- [31] V.M. Hong Ng et al., *J. Mater. Chem. A* 5 (7) (2017) 3039–3068.
- [32] P. Urbankowski et al., *Nanoscale* 8 (22) (2016) 11385–11391.
- [33] M. Li et al., *J. Am. Chem. Soc.* 141 (11) (2019) 4730–4737.
- [34] Y. Li et al., *Nat. Mater.* 19 (8) (2020) 1–6.
- [35] V. Kamysbayev et al., *Science* 369 (6506) (2020) 979–983.
- [36] S. Yang, et al., *Angew. Chem., Int. Ed.* 57 (47) (2018) 15491–15495.
- [37] J. Mei et al., *Sustain. Mater. Technol.* 25 (2020) e00156.
- [38] T. Li, et al., *Angew. Chem., Int. Ed.* 57 (21) (2018) 6115–6119.
- [39] W. Sun et al., *J. Mater. Chem. A* 5 (41) (2017) 21663–21668.
- [40] C. Xu et al., *Nat. Mater.* 14 (11) (2015) 1135–1141.
- [41] Z. Liu et al., *Nano Lett.* 16 (7) (2016) 4243–4250.
- [42] D. Geng et al., *Adv. Mater.* 29 (35) (2017) 1700072.
- [43] Y. Gogotsi, *Nat. Mater.* 14 (11) (2015) 1079–1080.
- [44] J. Jia et al., *ACS Nano* 11 (12) (2017) 12509–12518.
- [45] X. Sang et al., *Nat. Commun.* 9 (1) (2018) 2266.
- [46] X. Xiao et al., *Adv. Funct. Mater.* 29 (17) (2019) 1809001.
- [47] P. Urbankowski et al., *Nanoscale* 9 (45) (2017) 17722–17730.

- [48] J. Jeon et al., *ACS Nano* 12 (1) (2018) 338–346.
- [49] Z. Lin et al., *Small* 13 (35) (2017) 1700051.
- [50] X. Xiao et al., *ACS Nano* 11 (2) (2017) 2180–2186.
- [51] L. Gao et al., *Small Methods* 4 (8) (2020) 2000250.
- [52] Y. Gogotsi, B. Anasori, *ACS Nano* 13 (8) (2019) 8491–8494.
- [53] Q. Jiang et al., *Energy Storage Mater.* 27 (2020) 78–95.
- [54] J. Peng et al., *Chem* 5 (1) (2019) 18–50.
- [55] D. Zhang et al., *ACS Photonics* 9 (4) (2022) 1108–1116.
- [56] C. Si et al., *Nano Lett.* 16 (10) (2016) 6584–6591.
- [57] M. Je et al., *Thin Solid Films* 619 (2016) 131–136.
- [58] J. Guo et al., *J. Alloy. Compd.* 712 (2017) 752–759.
- [59] Y. Lee et al., *Phys. Chem. Chem. Phys.* 16 (47) (2014) 26273–26278.
- [60] B. Anasori et al., *Nat. Rev. Mater.* 2 (2) (2017) 16098.
- [61] K. Hantanasirisakul, Y. Gogotsi, *Adv. Mater.* 30 (52) (2018) e1804779.
- [62] M. Khazaei et al., *J. Mater. Chem. C* 5 (10) (2017) 2488–2503.
- [63] Y. Lee et al., *ACS Appl. Mater. Interfaces* 6 (16) (2014) 14724–14728.
- [64] L. Li, *J. Phys. Chem. C* 120 (43) (2016) 24857–24865.
- [65] X.-F. Yu et al., *RSC Adv.* 5 (39) (2015) 30438–30444.
- [66] X.H. Zha et al., *Nanoscale* 8 (11) (2016) 6110–6117.
- [67] X. Zhang et al., *Nanoscale* 7 (38) (2015) 16020–16025.
- [68] T. Hu et al., *Sci. Rep.* 5 (2015) 16329.
- [69] X. Sang et al., *ACS Nano* 10 (10) (2016) 9193–9200.
- [70] G.R. Berdiyrov, *EPL* 111 (6) (2015) 67002.
- [71] H. Wang et al., *Mater. Lett.* 160 (2015) 537–540.
- [72] A.D. Dillon et al., *Adv. Funct. Mater.* 26 (23) (2016) 4162–4168.
- [73] H. Lin et al., *J. Am. Chem. Soc.* 139 (45) (2017) 16235–16247.
- [74] S. Lu et al., *Adv. Sci.* 6 (9) (2019) 1801470.
- [75] Q. Xue et al., *Adv. Mater.* 29 (15) (2017) 1604847.
- [76] K. Hantanasirisakul et al., *Adv. Electron. Mater.* 2 (6) (2016) 1600050.
- [77] L. Gao et al., *ACS Nano* 16 (2) (2022) 3059–3069.
- [78] J.L. Hart et al., *Nat. Commun.* 10 (1) (2019) 522.
- [79] G.R. Berdiyrov, *AIP Adv.* 6 (5) (2016) 055105.
- [80] Y. Bai et al., *RSC Adv.* 6 (42) (2016) 35731–35739.
- [81] H. Chen et al., *Appl. Mater. Today* 21 (2020) 100800.
- [82] H. Chen et al., *Nanoscale* 13 (37) (2021) 15891–15898.
- [83] C. Wang et al., *Nanophotonics* 10 (10) (2021) 2617–2623.
- [84] V.N. Borysiuk et al., *Nanotechnology* 26 (26) (2015) 265705.
- [85] Z. Guo et al., *Phys. Chem. Chem. Phys.* 17 (23) (2015) 15348–15354.
- [86] B. Akuzum et al., *ACS Nano* 12 (3) (2018) 2685–2694.
- [87] C. Lee et al., *Science* 321 (5887) (2008) 385–388.
- [88] C. Si et al., *Phys. Rev. Lett.* 109 (22) (2012) 226802.
- [89] U. Yorulmaz et al., *Nanotechnology* 27 (33) (2016) 335702.
- [90] Z. Ling et al., *Proc. Natl. Acad. Sci. U.S.A.* 111 (47) (2014) 16676–16681.
- [91] Y.Z. Zhang et al., *Adv. Mater.* 32 (21) (2020) e1908486.
- [92] J. Pang et al., *Chem. Soc. Rev.* 48 (1) (2019) 72–133.
- [93] H. Lin et al., *Adv. Sci.* 5 (10) (2018) 1800518.
- [94] A. Iqbal et al., *Adv. Funct. Mater.* 30 (47) (2020) 2000883.
- [95] V.H. Nguyen et al., *Adv. Funct. Mater.* 30 (47) (2020) 1909504.
- [96] D.B. Velusamy et al., *Adv. Mater.* 31 (32) (2019) e1807658.
- [97] J. Chen et al., *Mater. Horiz.* 7 (7) (2020) 1828–1833.
- [98] K. Montazeri et al., *Adv. Mater.* 31 (43) (2019) e1903271.
- [99] H.S. Lim et al., *ACS Appl. Mater. Interfaces* 13 (21) (2021) 25400–25409.
- [100] Y. Zhang et al., *Mater Today Phys* 21 (2021) 100479.
- [101] Z. Wang et al., *Adv. Mater.* 30 (15) (2018) e1706656.
- [102] Y. Chen et al., *J. Phys. D: Appl. Phys.* 53 (48) (2020) 484001.
- [103] T. Jiang et al., *Appl. Surf. Sci.* 513 (2020) 145813.
- [104] M. Mariano et al., *Nanoscale* 8 (36) (2016) 16371–16378.
- [105] J. Xu et al., *Adv. Funct. Mater.* 26 (29) (2016) 5328–5334.
- [106] W. Ouyang et al., *Adv. Electron. Mater.* 6 (6) (2020) 2000168.
- [107] A. Ren et al., *Mater. Horiz.* 7 (7) (2020) 1901–1911.
- [108] C. Hu et al., *Chinese J. Chem.* 39 (8) (2021) 2141–2146.
- [109] Z. Kang et al., *Adv. Electron. Mater.* 3 (9) (2017) 1700165.
- [110] Z. Kang et al., *Sensors* 19 (5) (2019) 1099.
- [111] J. Jeon et al., *Adv. Funct. Mater.* 29 (48) (2019) 1905384.
- [112] Y. Yang et al., *ACS Nano* 13 (8) (2019) 8804–8810.
- [113] C. Hu et al., *Adv. Mater. Technol.* (2022) 2101639.
- [114] L. Luo et al., *Light-Sci. Appl.* 10 (1) (2021) 177.
- [115] Y. Sun et al., *IEEE Electron. Device Lett.* 42 (12) (2021) 1814–1817.
- [116] C. Yang et al., *Nanophotonics* 10 (16) (2021) 4133–4139.
- [117] S.Q. Yin et al., *J. Phys. D: Appl. Phys.* 55 (26) (2022) 265105.
- [118] W. Deng et al., *Adv. Opt. Mater.* 7 (6) (2019) 1801521.
- [119] J. Chen et al., *Adv. Funct. Mater.* 32 (24) (2022) 2201066.
- [120] S. Guo et al., *J. Phys. Chem. C* 124 (8) (2020) 4764–4771.
- [121] F. Cao et al., *J. Appl. Phys.* 129 (20) (2021) 204503.
- [122] H. Guo et al., *Small* 17 (34) (2021) e2101954.
- [123] M.-Y. Li et al., *ACS Appl. Nano Mater.* 4 (12) (2021) 13674–13682.
- [124] H. Ma et al., *Nanotechnology* 33 (7) (2021) 075502.
- [125] W. Song et al., *Adv. Mater.* 33 (27) (2021) e2101059.
- [126] W. Song et al., *Small* 17 (23) (2021) e2100439.
- [127] C. Yi et al., *Adv. Electron. Mater.* 7 (5) (2021) 2000955.
- [128] X. Zhang et al., *Mater. Design* 207 (2021) 109850.
- [129] J. Zhu et al., *Nano Res.* 14 (10) (2021) 3416–3422.
- [130] B. Li et al., *Adv. Mater.* 34 (17) (2022) e2201298.
- [131] H. Li et al., *J. Alloy. Compd.* 895 (2022) 162570.
- [132] V. Selamneni et al., *FlatChem* 33 (2022) 100363.
- [133] W. Song et al., *J. Alloy. Compd.* 909 (2022) 164816.
- [134] D. Xiong et al., *Nano Energy* 93 (2022) 106889.
- [135] Z.-Y. Yan et al., *IEEE J. Sel. Top. Quant.* 28 (2) (2022) 1–8.
- [136] X.Y. Zhou et al., *J. Mater. Chem. C* 10 (15) (2022) 5970–5980.
- [137] J. Zou et al., *ACS Appl. Mater. Interfaces* 14 (6) (2022) 8243–8250.
- [138] A. Iqbal et al., *Nano Converg.* 8 (1) (2021) 1–22.
- [139] M. Naguib et al., *Chem. Commun.* 50 (56) (2014) 7420–7423.
- [140] C.J. Zhang et al., *Chem. Mater.* 29 (11) (2017) 4848–4856.
- [141] V. Natu et al., *Angew. Chem., Int. Ed.* 131 (36) (2019) 12785–12790.
- [142] R.B. Rakhi et al., *Chem. Mater.* 27 (15) (2015) 5314–5323.
- [143] S. Chertopalov, V.N. Mochalin, *ACS Nano* 12 (6) (2018) 6109–6116.
- [144] N. Khatun et al., *Mater. Chem. Phys.* 278 (2022) 125651.
- [145] A. Pan et al., *J. Phys. Chem. Lett.* 10 (21) (2019) 6590–6597.
- [146] C. Cai et al., *ACS Appl. Mater. Interfaces* 13 (45) (2021) 54170–54184.
- [147] L. Gao et al., *ACS Nano* 15 (1) (2021) 954–965.
- [148] Y. Yang, et al., *SSRN Electron. J.* DOI:10.2139/ssrn.4057241 (2022).
- [149] B. Anasori et al., *Nanoscale Horiz.* 1 (3) (2016) 227–234.
- [150] M. Khazaei et al., *Phys. Chem. Chem. Phys.* 16 (17) (2014) 7841–7849.
- [151] D. Yi et al., *Opt. Lett.* 47 (1) (2022) 138–141.
- [152] Z. Yang et al., *Opt Laser Technol* 142 (2021) 107199.